



Elastic mechanics-based fixturing scheme optimization of variable stiffness structure workpieces for surface quality improvement

Guilong Li^{a,b}, Shichang Du^{a,b,*}, Delin Huang^{a,b}, Chen Zhao^{a,b}, Yafei Deng^{a,b}

^a State Key Lab of Mechanical System and Vibration, Shanghai Jiaotong University, Shanghai, 200240, China

^b School of Mechanical Engineering, Shanghai Jiaotong University, Shanghai, 200240, China

ARTICLE INFO

Keywords:

Fixturing scheme optimization
Elastic mechanics
Surface quality improvement
Variable stiffness structure
Face milling

ABSTRACT

The surface quality is quite important for many mechanical products. An improper fixturing scheme (i.e., magnitudes of clamping forces and fixture layout) leads to undesirable deformation of the workpiece, which will seriously affect the final quality of the machined surface, especially for the form accuracy. Current researches on fixturing scheme optimization have been mainly focused on rigid workpieces and flexible workpieces, however, seldom considered variable stiffness structure (VSS) workpieces. Besides, most existing fixturing scheme optimization models are derived based on the finite element method (FEM), which demands considerable time for computation. Therefore, there is a lack of an effective and efficient approach to improve the surface quality for VSS workpieces by fixturing scheme optimization. To this end, a novel systematic approach based on elastic mechanics is proposed in this paper. Firstly, a static cutting force model is developed to obtain the minimum clamping forces needed to maintain the fixturing stability. Secondly, by dividing the VSS workpiece into three kinds of characteristic regions, the analytical solutions of the elastic deformation induced by clamping forces are derived using elasticity theory. Thirdly, the optimization model is solved by the genetic algorithm, so as to minimize the maximum fixturing induced deformation of the surface to be machined. The effectiveness and efficiency of the proposed approach are verified by a face milling experiment on a four-cylinder engine block, and the final quality of the machined surface is improved by 9.1%.

1. Introduction

Continuous improvement in surface quality has become a major priority, particularly for corporations engaged in precision manufacturing. The machined surface quality has always been critical for satisfying the demands for superior performance, reliability, and durability [1]. The machined surface deviation is mainly caused by the irregular deformation of the workpiece during fixturing and material removing [2]. The machined surface quality is negatively related to the workpiece deformation induced by different clamping forces and fixture layouts [3]. Therefore, the choice of fixturing schemes, i.e., the magnitudes of clamping forces and positions of fixture elements, has a considerable impact on the final workpiece quality [4]. Current practices in fixturing scheme design, however, rely solely on the designer's experience and conservative guidelines, rather than systematic analysis [5]. Hence, it is an important yet urgent work for precision manufacturing industries to develop a systematic and scientific fixturing scheme optimization approach, so as to improve the machined surface

quality.

According to the structure stiffness, common workpieces are divided into flexible, rigid and variable stiffness structure (VSS) workpieces [6,7]. The stiffness magnitudes of flexible workpieces such as sheet metal, plates and beams are relatively low, whereas those of rigid workpieces such as non-cavity solid castings are relatively high. Both of flexible and rigid workpieces have uniform or slightly variable stiffness magnitudes due to their simple physical structures. With the rapid development of manufacturing industry, workpiece structures have been increasingly complex, and the stiffness magnitude of workpieces varies over a wide range. For instance, a four-cylinder engine block, made of gray cast iron HT250, is a typical partial thin-walled VSS workpiece [8]. As depicted in Fig. 1, the wall thickness varies from 5.5 mm to 75.5 mm [9] as the flexural stiffness varies from 234.87 N m² to 607537.41 N m² [10,11]. Whichever category a machining workpiece belongs to, an appropriate approach for deformation analysis is definitely essential for its fixturing scheme optimization. Most methods available for deformation analysis can be generally classified as numerical methods and

* Corresponding author. State Key Lab of Mechanical System and Vibration, Shanghai Jiaotong University, Shanghai, 200240, China.

E-mail addresses: lg152613@sjtu.edu.cn (G. Li), lovbin@sjtu.edu.cn (S. Du), cjwanan@sjtu.edu.cn (D. Huang), zhao_chen@sjtu.edu.cn (C. Zhao), phoenixdyf@sjtu.edu.cn (Y. Deng).

<https://doi.org/10.1016/j.precisioneng.2019.01.004>

Received 9 November 2018; Received in revised form 29 December 2018; Accepted 14 January 2019

Available online 19 January 2019

0141-6359/ © 2019 Elsevier Inc. All rights reserved.

Nomenclature

a_p (mm)	Axial cutting depth	d_1 (mm)	Distance from the first center line to front face
f_z (mm/tooth)	Feed per tooth	d_2 (mm)	Distance between two adjacent center line
β (°)	Helix angle of flank edge	d_3 (mm)	Length of Bridge region
V_s (rpm)	Spindle speed	H (mm)	Height of engine block
M	Number of micro elements of each tooth	R_b (mm)	Radius of cylinder bore
N	Number of teeth	A_B (mm ²)	Top surface area of Bridge region
$\theta_{j,l}$ (°)	Radial immersion angle of the l^{th} micro element of the j^{th} tooth ($j = 1, 2, \dots, N; l = 1, 2, \dots, M$)	S_i	Virtual plane
$\theta_{1,0}$ (°)	Angular displacement of the bottom of the first tooth	λ (mm)	Distance between virtual plane to top surface
$\theta_{st}; \theta_{ex}$ (°)	Starting cut angle; exiting cut angle	α_S	Fitness weight function
R_c (mm)	Ideal cutter radius	p_c	Crossover probability
$K_r; K_t; K_a$	Radial, tangential and axial cutting parameter coefficients	ζ_R	Safety coefficient
$A_x; A_y; A_z$	Corresponding undetermined coefficients	$dx; dy; h$ (mm)	Length, width and height of the micro element of elastic plate
$B_x; B_y; B_z$	Substituting undetermined coefficients	p_m	Mutation probability
K_{sc}	Stress concentration coefficient	g_c	Convergence generation
D (N·m ²)	Flexural stiffness of elastic plate	S_0 (mm)	Threshold of the maximum deformation
$D(x)$ (N·m ²)	Flexural stiffness of Span region along X-axis	$L_a; L_b$ (mm)	Length and width of Span region
$F_x; F_y; F_z$ (N)	Cutting forces along X,Y, and Z axes	P	External load function
$F_{A,x}; F_{A,y}; F_{A,z}$ (N)	Average cutting forces along X,Y, and Z axes	ϕ	Stress function
$F_{C,x}; F_{C,y}; F_{C,z}$ (N)	Optimal clamping forces along X,Y, and Z axes	d_B (mm)	minimum distance from the origin to mass point of X-axis with zero vertical displacement
$\sigma_{max}; \sigma_{avg}$ (MPa)	Maximum normal stress; average normal stress	d_p (mm)	Bias of external load
$\varepsilon_x; \varepsilon_y; \gamma_{xy}$	Normal strain along X-axis; normal strain along Y-axis; shear strain of mid-surface	$l(x)$	Thickness function of Bridge region along X-axis
$\sigma_x; \sigma_y; \sigma_z$ (MPa)	Normal stress along X,Y, and Z axes	T (N·m)	Balanced torque
$u; v; w$ (mm)	Displacements along X,Y, and Z axes	M_t (N·m)	Pre-tightening torque
$\kappa_x; \kappa_y; \kappa_{xy}$	Curvatures of mid-surface along X-axis; curvatures of mid-surface along Y-axis; twist rate of mid-surface	K_t	Pre-tightening coefficient
a (mm)	Length of engine block	D_b (mm)	Diameter of the bolt
b (mm)	Width of engine block	E (MPa)	Elastic modulus
		ν	Poisson ratio

analytical ones [12]. Due to the superior operability and applicability, fixturing scheme optimization models based on numerical methods, with the represent of finite element method (FEM), have been well studied in recent few decades. However, most of the existing numerical methods are computationally demanding [13]. Moreover, the numerical calculation processes are in a black box [14], which means it is not intuitive that how the deformation is calculated, and the physical insights are limited [15]. In contrast, analytical methods with the represent of elastic mechanics analysis can overcome the above disadvantages.

For flexible workpieces, based on the “N-2-1” locating principle

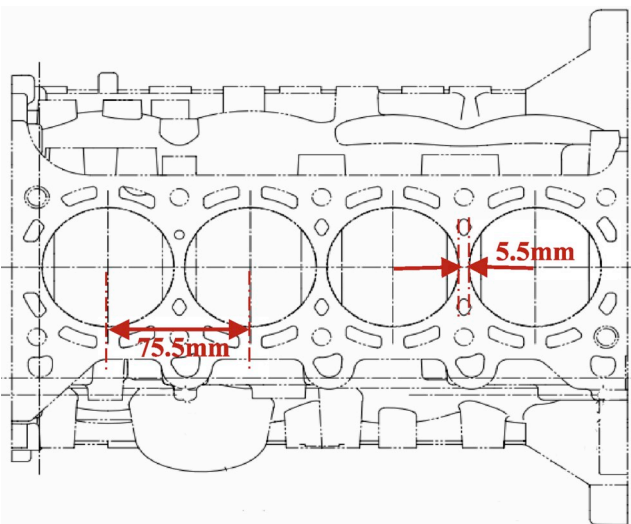


Fig. 1. Top view of a four-cylinder engine block.

dealing with fixturing scheme design for sheet metal, Cai and Hu [16] presented an approach using FEM and nonlinear programming methods to find the optimal number of locating points “N”, such that the total deformation of the flexible sheet metal was minimized. Liu et al. [17] proposed an accurate cutting force model along with a finite element model to optimize the positions of the locators in peripheral milling of a thin-walled workpiece. Chen et al. [18] established a multi-objective model to reduce the degree of deformation induced by fixturing for a hollow workpiece. The FEM was employed to analyze the deformation, and a heuristic algorithm was developed to solve the optimization model. Rai and Xirouchakis [19] presented a comprehensive FEM based verification model and associated tools for milling process plan, and predicted the thin wall deflections and elastic–plastic deformations of workpiece during machining. Bellifa et al. [20] developed a novel first-order shear deformation theory for bending and dynamic behaviors of functionally graded plates. Based on the third-order shear deformation beam theory, Ebrahimi and Barati [21] presented a Navier-type solution for the free vibration characteristics of functionally graded nanobeams. Shan et al. [22] established the relationship between the milling force and the tool inclination angle in ball-end milling by using the theoretical and experimental methods. The effect of tool inclination angle on both the milling forces and the elastic deformation of thin-walled workpieces was analyzed by FEM, and the optimal tool inclination angle leading to the minimum milling forces and deformation was found.

For rigid workpieces, Kaya and Ozturk [23] proposed a FEM based workpiece-fixture layout verification approach with the application of frictional contact and chip removal effects. By using kinematic analysis, Carlson [24] derived a quadratic sensitivity equation considering the relationship between position error in locators and the resulting displacement of the rigid workpiece held by the fixture. Sadd [25] investigated plane stress non-homogeneous isotropic elasticity problems

by presenting some simple solutions described in Cartesian coordinates. By considering the parameters of milling and tool wear, Pimenov et al. [26] proposed an analytical model of flatness deviation to determine the angular compliance values of a face milling system. Wojciechowski [27] investigated the machined surface roughness with respect to the machining system dynamics for the monolithic torus milling process of hardened steel. A surface roughness model was developed considering the quantitative influence of cutting forces and cutter displacements, which revealed a strong dependence of the real surface roughness parameters on dynamic cutter displacements.

To this day, however, limited research works have been focused on VSS workpieces. Based on computer-aided fixture design verification (CAFDV) techniques, Kang et al. [28,29] introduced a comprehensive framework using both geometric and kinetic models to verify the fixturing stability and locating accuracy. By using FEM, Liao and Hu [30,31] proposed an integrated model of a fixture-workpiece system considering fixture stability, verified by a case study of a V-type engine block. Gong et al. [32] proposed a FEM based X-ray optics bending mechanism design to suppress the surface errors by studying the mechanical state and the bending resolving power.

In summary, numerical methods for elastic deformation of workpiece have been well studied even though there are several shortcomings that can be overcome by analytical methods, whereas published analytical methods have been confined within the deformation analyses of flexible and rigid workpieces. The shortage of analytical methodologies for deformation calculation has imposed a significant constraint on fixturing scheme optimization of VSS workpieces, which will eventually influence the final quality of machined surfaces.

In this paper, a novel analytical approach based on elastic mechanics is proposed to optimize the fixturing schemes of VSS workpieces for surface quality improvement. The basic idea is to minimize the clamping forces needed for stable fixturing by a static cutting force model, and derive the analytical solution of the elastic deformation induced by clamping forces using elasticity theory, and then solve the optimization model by heuristic algorithms to minimize the total fixturing induced deformation of the surface to be machined. The genetic algorithm (GA) is a stochastic, heuristic and robust optimization method based on biological reproduction processes [33,34]. Since GA only deals with the fixture design variables and fitness value of the objective function for a specific fixturing scheme, no more auxiliary information is required [35,36]. Hence, it is ideally suited to implement GA for solving the fixturing scheme optimization problem.

The remainder of the paper is organized as follows. Section 2 shows the specific procedures of the proposed approach, including force analysis, elasticity analysis and the fixture layout optimization model. In Section 3, the effectiveness and efficiency of the proposed approach is demonstrated by a machining experiment on a type of four-cylinder engine block called B12, and the experimental results from the optimized scheme are compared with those from the initial scheme. A FEM-based simulation of the machining process is presented as well. Section 4 is devoted to the conclusion from this study.

2. The proposed approach

The framework of the proposed approach is shown in Fig. 2, and the main steps of this approach are described as follows.

Step 1: Develop an exponential instantaneous model of static cutting force in face milling process, in order to calculate the minimum magnitudes of clamping forces needed for maintaining the physical stability of the machining system.

Step 2: Analyze the fixturing induced deformation of the top surface of a typical VSS workpiece. Based on the superposition principle [37], a division strategy is implemented to divide the VSS elastomer into three different kinds of characteristic regions denoted by Pier, Span and Bridge respectively. According to the classical 3-2-1

locating principle, when a single clamping force is perpendicularly loaded on the flank of a Pier or a Span region, the analytical solutions of deformation and section stress field are derived using elastic mechanics. The deformation of a Bridge region is calculated by taking the stress field of Pier-Bridge section as the input load. Each region is analyzed individually and the top surface displacement fields of each region are superimposed as the total deformation of the top surface induced by fixturing.

Step 3: Build the fixturing scheme optimization model for VSS workpieces. The objective is to minimize the flatness of the top surface after fixturing but before machining. The main constraints are fixturing stability and practical operation feasibility. Since the relationship between fixturing scheme and fixturing induced surface deformation is quite complex, which makes this problem a nonlinear programming, GA is employed to solve this optimization model.

2.1. Force analysis

The primary function of a fixture is to keep the workpiece in the desired position and orientation during the manufacturing process [12]. Force analysis is concerned with checking that the forces applied by the fixtures are sufficient to maintain static equilibrium of the workpiece in the presence of cutting forces. This study is mainly focused on the face milling process, one of the most commonly used surface machining processes in manufacturing industry. Material removal is a complex dynamic process due to periodic forced vibrations [38,39]. Nevertheless, once the frequency of cutting forces, i.e. the cutting tooth passing frequency [40,41], is far away from each one of the chatter frequencies of the fixture-workpiece system, the impact of forced vibrations on the final quality of a machined surface is quite minor and thus negligible [31]. Moreover, Hence, a static cutting force model for face milling process is derived to determine the minimum magnitudes of clamping forces.

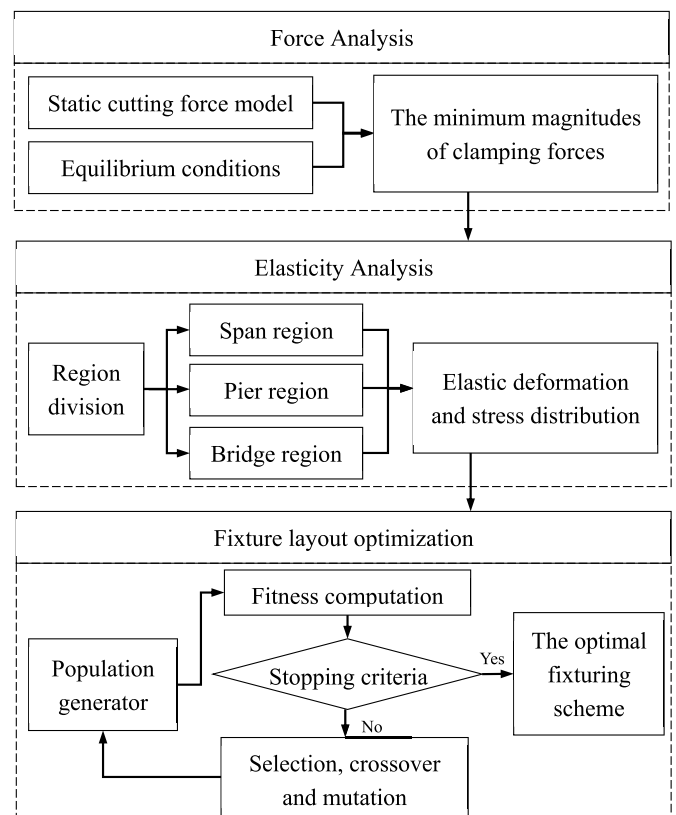


Fig. 2. Framework of the proposed approach.

2.1.1. Static cutting force model

In general cases, the milling system can be simplified to a two-degree-of-freedom vibration systems [42] as shown in Fig. 3(a). Therein, θ_{st} is the starting cut angle while θ_{ex} is the exiting cut angle. Supposing that there are a total of N teeth on the milling cutter and the cutting edge of each tooth is divided into M micro elements, for the l^{th} micro element of the cutting edge of j^{th} tooth engaged with the workpiece, the radial immersion angle [42] is denoted as

$$\theta_{j,l} = \theta_{1,0} + \frac{2\pi(j-1)}{N} + \frac{a_p l \tan \beta}{MR_c} \quad (1)$$

where $\theta_{1,0}$, ν , β and R_c denote angular displacement of the bottom of the first cutting edge, axial cutting depth, helix angle of the flank edge and the ideal cutter radius respectively, for $j = 1, 2, \dots, N$ and $l = 1, 2, \dots, M$.

As illustrated in Fig. 3(b), the cutting force on the micro element dF can be decomposed into three mutually perpendicular components, i.e. the axial, radial and tangential force, denoted by dF_a , dF_r , and dF_t , respectively.

Superimposing the force components on all cutting edges engaged with the workpiece after coordinate transformation, yields

$$\begin{cases} F_x = \sum_{j=1}^N \sum_{l=1}^M [-dF_{t,j,l} \cos \theta_{j,l} - dF_{r,j,l} \sin \theta_{j,l}] \\ F_y = \sum_{j=1}^N \sum_{l=1}^M [dF_{t,j,l} \sin \theta_{j,l} - dF_{r,j,l} \cos \theta_{j,l}] \\ F_z = \sum_{j=1}^N \sum_{l=1}^M dF_{a,j,l} \end{cases} \quad (2)$$

For the exponential instantaneous model [43,44], during each round of the milling cutter, the average cutting force components along the X, Y, and Z axes can be calculated by

$$\begin{cases} F_{A,x} = \frac{a_p N}{2\pi} K_r f_z^{A_x} \int_{\theta_{st}}^{\theta_{ex}} (\sin \theta)^{1-A_x} d\theta \\ F_{A,y} = \frac{a_p N}{2\pi} K_t f_z^{A_y} \int_{\theta_{st}}^{\theta_{ex}} (\sin \theta)^{1-A_y} d\theta \\ F_{A,z} = \frac{a_p N}{2\pi} K_a f_z^{A_z} \int_{\theta_{st}}^{\theta_{ex}} (\sin \theta)^{A_z} d\theta \end{cases} \quad (3)$$

where K_r , K_t and K_a denote the radial, tangential and axial cutting parameter coefficients respectively while A_x , A_y and A_z are the corresponding undetermined coefficients, and f_z is the feed per tooth.

By taking the logarithm on both sides of Eq. (3), it can be derived that

$$\ln \left(\frac{F_{A,q}}{a_p N} \right) = A_q \ln f_z + B_q \quad (4)$$

$$\begin{cases} K_r = \frac{2\pi e^{B_x}}{\int_{\theta_{st}}^{\theta_{ex}} (\sin \theta)^{1+A_x} d\theta} \\ K_t = \frac{2\pi e^{B_y}}{\int_{\theta_{st}}^{\theta_{ex}} (\sin \theta)^{1+A_y} d\theta} \\ K_a = \frac{2\pi e^{B_z}}{\int_{\theta_{st}}^{\theta_{ex}} (\sin \theta)^{A_z} d\theta} \end{cases} \quad (5)$$

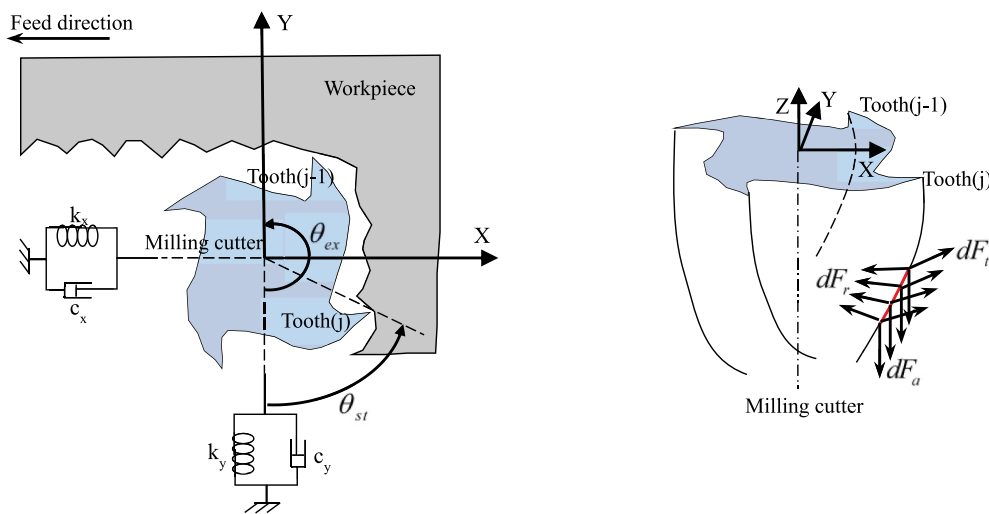
where B_q , for $q = x, y, z$, is another group of undetermined coefficients substituting K_r , K_t and K_a . Since Eq. (4) is obviously a group of linear equations, both A_q and B_q can be obtained by the least square method [45] through multiple sets of experimental tests of cutting forces using different machining parameters. Thus, the average cutting force components along each axis can be calculated by Eq. (3) respectively.

2.1.2. Equilibrium conditions

The main purpose of a fixturing scheme is to accurately locate, adequately support, and properly constrain the workpiece during machining. This purpose can be achieved by strategically placing fixture elements i.e. locator pins, supports and clamps, around the workpiece and applying the clamping forces with appropriate magnitude. Excessive clamping forces result in unnecessary deformation and poor machining quality of workpieces, whereas insufficient ones cannot satisfy the fixturing stability that could lead to dangerous accidents. Hence, it is necessary to scientifically determine the magnitudes of the clamping forces. As for conventional practice in fixturing scheme design, the magnitudes of the clamping forces are artificially estimated mainly based on the experience of similar types of fixture [46]. In this paper, by regarding the workpiece-fixture as an integrated system, the static equilibrium conditions for fixturing stability are analyzed and calculated. In order to make the clamping reliable, the calculated theoretical magnitudes of clamping forces just satisfying the equilibrium conditions should be multiplied by a safety coefficient ζ_R , which generally ranges from 2.5 to 3 for roughing [47] while from 1.5 to 2 for finishing [48,49]. It can be formulated as follows.

$$F_{C,q} = \zeta_R F_{A,q} \quad (6)$$

The clamping force along each direction is provided by the transmission rod of a clamping chuck device. For instance, a chuck device with three different clamps is shown in Fig. 4, supposing that the



(a) Simplified dynamic milling system (b) Components of the milling force

Fig. 3. Cutting force modeling for milling process.

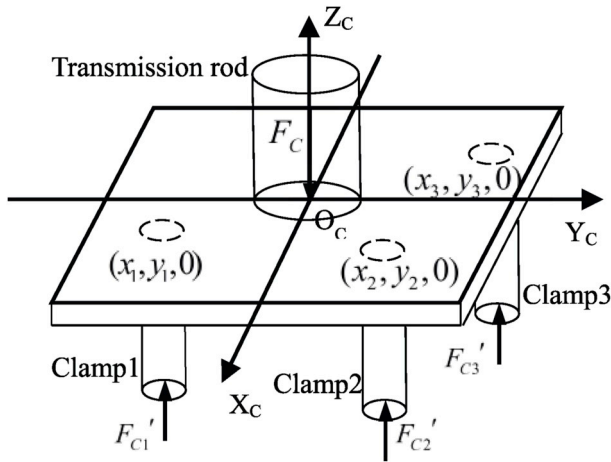


Fig. 4. Force distribution of the clamping chuck device.

coordinates of these three clamps are $(x_1, y_1, 0)$, $(x_2, y_2, 0)$ and $(x_3, y_3, 0)$ respectively, w.r.t. the three-dimensional Cartesian coordinate system (CCS) $O_c X_c Y_c Z_c$. Thus according to the static equilibrium conditions, the force distribution of each clamps can be obtained by solving the following equation set.

$$\begin{cases} F_c = F_{c1} + F_{c2} + F_{c3} \\ F_{c1}|x_1| + F_{c2}|x_2| - F_{c3}|x_3| = 0 \\ F_{c1}|y_1| - F_{c2}|y_2| - F_{c3}|y_3| = 0 \end{cases} \quad (7)$$

Analogously, the clamping force distribution of other chuck devices

with two or four clamps can be calculated as well. The optimized clamping forces will be the load input of the elasticity analysis model and therefore play an important role in the proposed approach.

2.2. Elasticity analysis

For VSS workpieces, the fixturing induced deformation is hard yet important to analyze. With a simplified four-cylinder engine block as a typical example of VSS workpieces, a novel systematic model based on elastic mechanics is derived for deformation analysis and related analytical solutions are given in this study. Since the fixturing induced plastic deformation is negligible [12,29], the deformation appearing in the following text is deemed as elastic unless otherwise stated.

2.2.1. Region division

When a VSS workpiece is loaded with different clamping forces during fixturing before the machining process, the deformation will be irregular and complicated for analysis and control due to the variable stiffness, which is unfavorable for the machined surface quality. Unfortunately, it is practically impossible to analytically calculate the displacement field for a VSS workpiece as a whole. Thus, a region division strategy based on elastic mechanics is proposed in this paper.

Taking a four-cylinder engine block as an example, this paper is mainly focused on fixturing scheme optimization for the face milling process with a 3-2-1 locating principle. Constrained by practical processing conditions, the positions of locator-clamp pairs on the secondary and tertiary locating datum planes are hardly changeable. In other words, fixture layout optimization is concentrated on the primary locating datum plane and its opposite plane, containing three pairs of locator-clamp. One of the most prominent geometric features of an

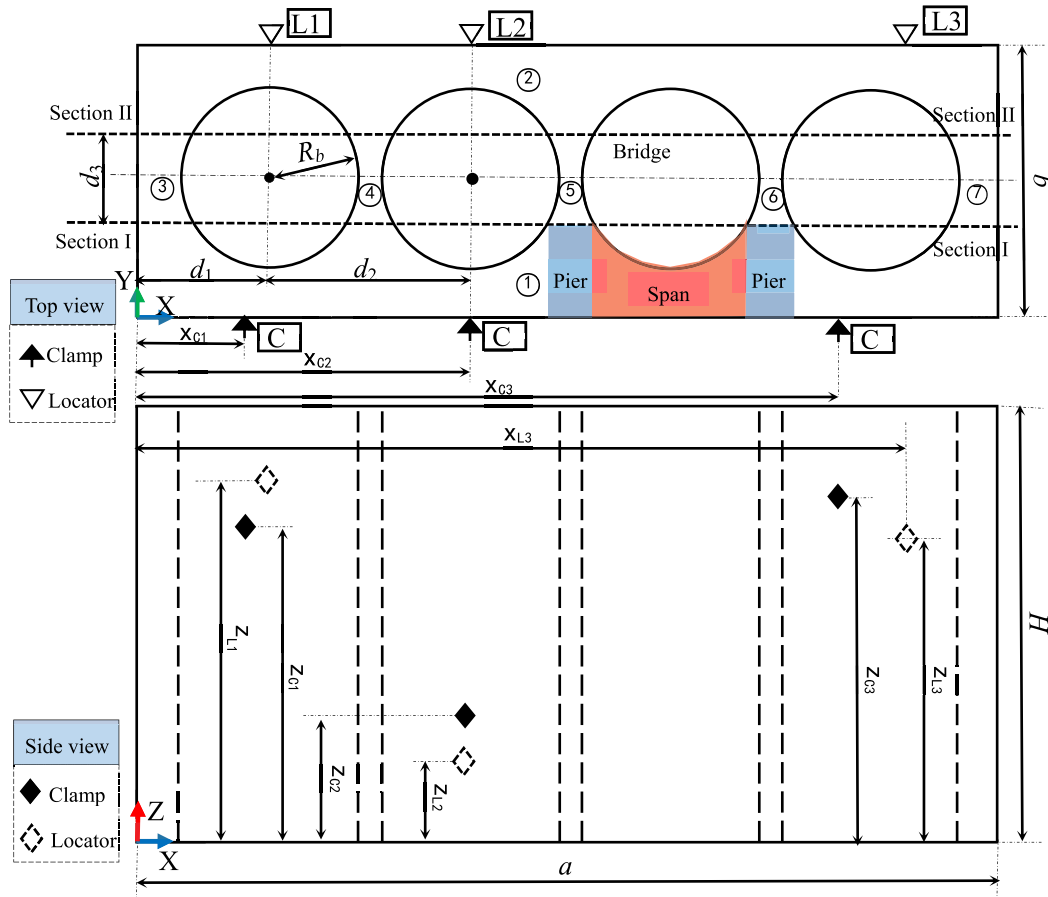


Fig. 5. Region division of a simplified four-cylinder engine block.

engine block is that it contains multiple closely spaced cylinder bores resulting in significant and continuous variation in wall thickness. In the case of isotropic elastic modulus of material, both flexural and compressive stiffness are directly dependent on wall thickness of the workpiece, and that is how the variable stiffness structure forms. For a simplified engine block retaining its most important geometric features (see Fig. 5), it is divided into seven numbered regions by two parallel sections denoted by Section I and II respectively, where d_j (for $j = 1,2,3$) are all given distance parameters while a, b, H and R_b donate the length, width, height of the engine block and the radius of the cylinder bore respectively.

Suppose that three clamping forces are perpendicularly loaded on the flank of region 1 while the flank of region 2 is contacting with three corresponding locators. Based on the stiffness features, these two regions can be further subdivided into several sub-regions, termed as Span regions and Pier regions respectively. The remaining regions from 3 to 7 are termed as Bridge regions. Since the applying position of a clamping force belongs to the flank of either a Span region or a Pier region, the deformation of these two kinds of regions induced by each single force is calculated individually using elastic mechanics, while the deformation of Bridge regions is calculated based on the elasticity analysis of Span and Pier regions. According to the superposition principle, the displacement fields of each region can be superposed as the final displacement field after fixturing. Of note is that the deformation of a VSS workpiece with other geometric features and locating principles can be calculated by an elasticity analysis model akin to the proposed one as well, which, however, is not within the scope of this paper.

2.2.2. Span region

It is the main difference between the classic elastic plate with uniform thickness and the Span region that the flexure stiffness of elastomer is constant or not. Thus, the Span region can be deemed as an elastic plate with variable stiffness. When a clamping force is perpendicularly loaded on the flank of a Span region connecting with two adjacent Pier regions (see Fig. 6), termed as a Pier-Span-Pier system, the deformation and stress field should be calculated within this system. The physical geometry of the system is discontinuous due to the portion of cylinder bore in Span region, therefore the localized stress will be high in the Pier-Bridge sections. This phenomenon is academically called stress concentration [50,51] and generally formulated as

$$K_{sc} = \frac{\sigma_{max}}{\sigma_{avg}} \tag{8}$$

where K_{sc} , σ_{max} and σ_{avg} refer to the stress concentration coefficient, the maximum normal stress and the average normal stress respectively. For a specific physical structure, K_{sc} is a constant which can be obtained by photo-physical experiments or empirical formulas [52].

An elastic micro element of elastic plate is shown in Fig. 7, where dx, dy and h denote the length, width and height of the micro element respectively.

According to Ref. [37], the internal moment of this micro element is given by

$$\begin{cases} M_x = \int_{-\frac{h}{2}}^{\frac{h}{2}} \sigma_x z dz = -D \left(\frac{\partial^2 w}{\partial x^2} + \nu \frac{\partial^2 w}{\partial y^2} \right) = D(\kappa_x + \nu \kappa_y) \\ M_y = \int_{-\frac{h}{2}}^{\frac{h}{2}} \sigma_y z dz = -D \left(\frac{\partial^2 w}{\partial y^2} + \nu \frac{\partial^2 w}{\partial x^2} \right) = D(\kappa_y + \nu \kappa_x) \\ M_{xy} = \int_{-\frac{h}{2}}^{\frac{h}{2}} \tau_{xy} z dz = -D(1 - \nu) \frac{\partial^2 w}{\partial x \partial y} = D(1 - \nu) \kappa_{xy} \end{cases} \tag{9}$$

where D is the flexural stiffness defined as

$$D = \frac{Eh^3}{12(1 - \nu^2)} \tag{10}$$

Denoting the external load function as $q(x, y)$, the deflection

equation can be represented as

$$\frac{\partial^4 w}{\partial x^4} + 2 \frac{\partial^4 w}{\partial x^2 \partial y^2} + \frac{\partial^4 w}{\partial y^4} = \frac{q}{D} \tag{11}$$

The boundary conditions for a single Span region can be formulated as

$$\begin{cases} w = 0, \frac{\partial^2 w}{\partial x^2} = 0 & \text{for } x = 0, L_a \\ M_y = 0, M_{yx} = 0 & \text{for } y = 0, L_b \end{cases} \tag{12}$$

where $L_a = \sqrt{4R_b^2 - d_3^2}$ and $L_b = H$ are the length and width of the Span region respectively and both known constants.

Using the properties of the double trigonometric series [53,54], under the premise of satisfying the boundary conditions given by Eq. (12), the double trigonometric series expansion is applied to the deflection $w(x, y)$ and the external load $q(x, y)$ respectively, and eventually the analytical solution to the deflection is obtained in the form of a function of the given load.

$$w(x, y) = \sum_{m=1}^{\infty} \sum_{n=1}^{\infty} A_{mn} \sin \frac{m\pi x}{L_a} \sin \frac{n\pi y}{L_b} \tag{13}$$

$$q(x, y) = \sum_{m=1}^{\infty} \sum_{n=1}^{\infty} C_{mn} \sin \frac{m\pi x}{L_a} \sin \frac{n\pi y}{L_b} \tag{14}$$

where A_{mn} and C_{mn} are two undetermined coefficients and both of them can be obtained by the following procedures.

Substituting Eq. (13) into Eq. (11), yields

$$\pi^4 D \sum_{m=1}^{\infty} \sum_{n=1}^{\infty} \left(\frac{m^2}{L_a^2} + \frac{n^2}{L_b^2} \right)^2 A_{mn} \sin \frac{m\pi x}{L_a} \sin \frac{n\pi y}{L_b} = q(x, y) \tag{15}$$

The orthogonality of trigonometric functions is formulated as

$$\int_0^{\frac{L_a}{2}} \sin \frac{m\pi x}{L_a} \sin \frac{m'\pi x}{L_a} dx = \begin{cases} 0 & \text{for } m \neq m' \\ \frac{L_a}{2} & \text{for } m = m' \end{cases} \tag{16}$$

Multiplying both sides of Eq. (14) by $\sin \frac{m\pi x}{L_a} \sin \frac{n\pi y}{L_b}$, and integrating in $[0, L_a]$ and $[0, L_b]$ w.r.t. x and y respectively, yields

$$\int_0^{L_b} \int_0^{L_a} q(x, y) \sin \frac{m\pi x}{L_a} \sin \frac{n\pi y}{L_b} dx dy = \frac{L_a L_b}{4} C_{mn} \tag{17}$$

It can be derived that

$$C_{mn} = \frac{4}{L_a L_b} \int_0^{L_b} \int_0^{L_a} q(x, y) \sin \frac{m\pi x}{L_a} \sin \frac{n\pi y}{L_b} dx dy \tag{18}$$

Substituting Eq. (18) into Eq. (14), and then substituting the new equation into Eq. (15), the deflection function can be further formulated as

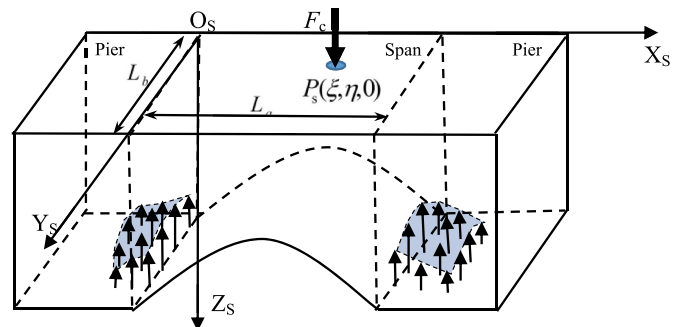


Fig. 6. The Pier-Span-Pier system loaded with a perpendicular clamping force.

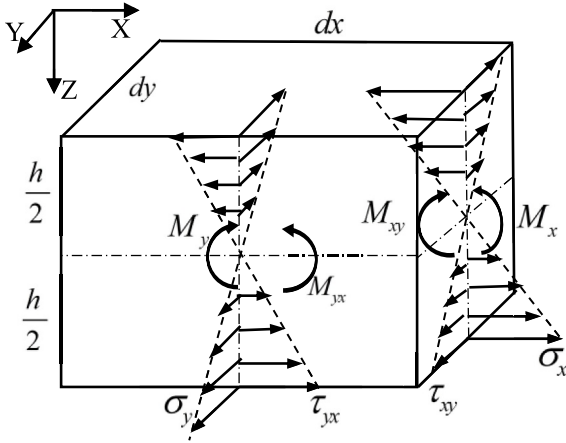


Fig. 7. Illustration of the micro element of elastic plate.

When a concentrated clamping force F_c , as a special case of external load, is perpendicularly exerted on the point P_s whose coordinates are $(\xi, \eta, 0)$ w.r.t. the $CCSO_S X_S Y_S Z_S$, the deflection can be rewritten as

$$w = \frac{4F_c}{\pi^4 L_a L_b D} \sum_{m=1}^{\infty} \sum_{n=1}^{\infty} \frac{\sin \frac{m\pi\xi}{L_a} \sin \frac{n\pi\eta}{L_b}}{\left(\frac{m^2}{L_a^2} + \frac{n^2}{L_b^2}\right)^2} \sin \frac{m\pi x}{L_a} \sin \frac{n\pi y}{L_b} \quad (23)$$

Since the thickness of a Span region $h(x)$ varies continuously along the X-axis direction, it can be formulated as

$$h(x) = \frac{b}{2} - \sqrt{R_b^2 - \left(\frac{L_a}{2} - x\right)^2} \quad (24)$$

The flexural stiffness $D(x)$ is consequently derived as

$$D(x) = \frac{E}{12(1-\nu^2)} \left[\frac{b}{2} - \sqrt{R_b^2 - \left(\frac{L_a}{2} - x\right)^2} \right]^3 \quad (25)$$

Hence, the analytical solution to the deflection function of the Span region is formulated as

$$w = \frac{48F_c(1-\nu^2)}{\pi^4 L_a L_b E \left[\frac{b}{2} - \sqrt{R_b^2 - \left(\frac{L_a}{2} - x\right)^2} \right]^3} \sum_{m=1}^{\infty} \sum_{n=1}^{\infty} \frac{\sin \frac{m\pi\xi}{L_a} \sin \frac{n\pi\eta}{L_b}}{\left(\frac{m^2}{L_a^2} + \frac{n^2}{L_b^2}\right)^2} \sin \frac{m\pi x}{L_a} \sin \frac{n\pi y}{L_b} \quad (26)$$

$$\begin{aligned} & \sum_{m=1}^{\infty} \sum_{n=1}^{\infty} \left(\frac{m^2}{L_a^2} + \frac{n^2}{L_b^2}\right)^2 A_{mn} \sin \frac{m\pi x}{L_a} \sin \frac{n\pi y}{L_b} \\ &= \sum_{m=1}^{\infty} \sum_{n=1}^{\infty} B_{mn} \sin \frac{m\pi x}{L_a} \sin \frac{n\pi y}{L_b} \end{aligned} \quad (19)$$

Therein, B_{mn} is another coefficient given by

$$B_{mn} = \frac{4}{\pi^4 D L_a L_b} \int_0^{L_b} \int_0^{L_a} q(x, y) \sin \frac{m\pi x}{L_a} \sin \frac{n\pi y}{L_b} dx dy \quad (20)$$

For any $\{(x, y) | 0 < x < L_a, 0 < y < L_b\}$, to ensure Eq. (19) always holds, coefficients of the trigonometric series on both sides of Eq. (19) should be correspondingly equal, thus

$$A_{mn} = \frac{4 \int_0^{L_b} \int_0^{L_a} q(x, y) \sin \frac{m\pi x}{L_a} \sin \frac{n\pi y}{L_b} dx dy}{\pi^4 D L_a L_b \left(\frac{m^2}{L_a^2} + \frac{n^2}{L_b^2}\right)^2} \quad (21)$$

Substituting Eq. (21) into Eq. (13), yields

$$w = \frac{4}{\pi^4 L_a L_b D} \sum_{m=1}^{\infty} \sum_{n=1}^{\infty} \frac{\int_0^{L_b} \int_0^{L_a} q(x, y) \sin \frac{m\pi x}{L_a} \sin \frac{n\pi y}{L_b} dx dy}{\left(\frac{m^2}{L_a^2} + \frac{n^2}{L_b^2}\right)^2} \sin \frac{m\pi x}{L_a} \sin \frac{n\pi y}{L_b} \quad (22)$$

Example I. An example is given in order to illustrate the proposed approach to calculating the fixturing induced deformation of the Span region before the machining process. A concentrated clamping force F_c known as 150 N, is perpendicularly exerted on a point of the flank of a Span region, namely, $P_s(20, 170, 0)$ w.r.t. the local $CCSO_S X_S Y_S Z_S$. Supposing the material of the workpiece is the gray cast iron HT250, dimensions of the Span region and necessary information of material are given in Table 1.

According to Eq. (26), the deflection w of the Span region is calculated as

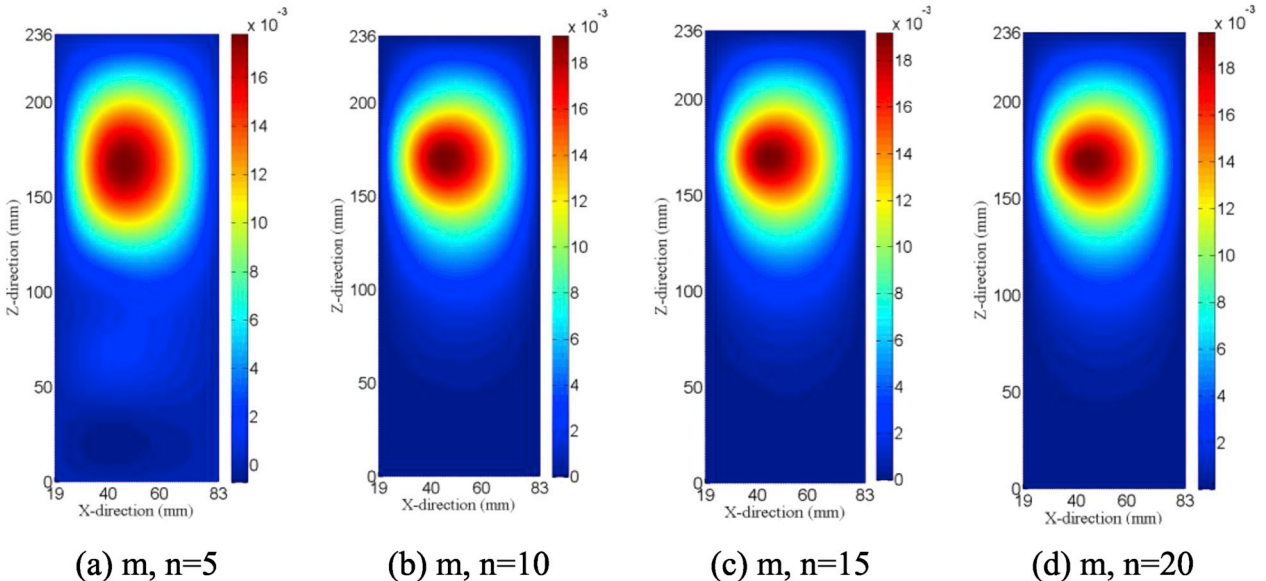


Fig. 8. Displacement field of the flank of a Span region loaded with a perpendicular concentrated force calculated by the double trigonometric series method.

$$w = \frac{48 \times 150(1 - 0.27^2)}{64 \times 236 \times 1.4 \times 10^5 \pi^4 \left[\frac{108}{2} - \sqrt{35^2 - \left(\frac{64}{2} - x\right)^2} \right]^3} \sum_{m=1}^{\infty} \sum_{n=1}^{\infty} \frac{\sin \frac{20m\pi}{64} \sin \frac{170n\pi}{236}}{\left(\frac{m^2}{64^2} + \frac{n^2}{236^2}\right)^2} \sin \frac{m\pi x}{64} \sin \frac{n\pi y}{236}$$

Through the MATLAB programming procedure, the displacement field is obtained as shown in Fig. 8. When the superposition times exceed 15, i.e. both m and n are larger than 15, the displacement field remains approximately constant, which demonstrates the fast convergence of the double trigonometric series method for elasticity analysis of the Span region. The maximum deformation induced by the clamping force in this example is 0.020 mm.

2.2.3. Pier region

The Pier region is the only one of the three types of regions that does not need to consider the effect of variable stiffness, and its compressive stiffness is relatively large. Nevertheless, the elastic analysis of this region is still important. The reasons are described as follows. On the one hand, the top surface of a Pier region is an indispensable part of that of an engine block, which is the object of face milling. The fixturing induced deformation of the Pier region will influence the surface quality after face milling process. On the other hand, the Pier region is directly connected to the Bridge region. The analysis of the stress field in the Pier region is the basis for deriving the analytical solution to the stress on the Pier-Bridge section, which is an important part of the input for elastic analysis of the Bridge region.

In this paper, the elasticity analysis of Pier region is deemed as an extension of the semi-infinite elastomer problem, taking the actual physical boundaries into consideration. An elastic semi-infinite space (see Fig. 9) can be defined as $\{(x, y, z) | -\infty < x, y < +\infty, z \leq 0\}$, w.r.t. the local $CCSO_P X_P Y_P Z_P$.

Considering a clamping force is perpendicularly exerted on the flank of a Pier region, within a certain range, this problem can be equivalent to elasticity analysis of the elastic semi-infinite space whose boundary is loaded with a normal concentrated force, in other words, the classic Boussinesq problem [55,56]. Taking the force applying point as the origin, the analytical solution to the stress field in polar coordinate form [56] is given by Eq. (27).

$$\begin{cases} \sigma_r = \frac{F_c}{2\pi} \left[\frac{1-2\nu}{R(R+z)} - \frac{3zr^2}{R^5} \right] \\ \sigma_\theta = \frac{F_c(1-2\nu)}{2\pi} \left[\frac{z}{R^3} - \frac{1}{R(R+z)} \right] \\ \sigma_z = -\frac{3F_c z^3}{2\pi R^5} \\ \tau_{rz} = -\frac{3F_c r z^2}{2\pi R^5} \end{cases} \quad (27)$$

And the displacement field is given as well.

$$\begin{cases} u = \frac{(1+\nu)F_c}{2\pi E} \left[\frac{rz}{R^3} - (1-2\nu)\frac{r}{R(R+z)} \right] \\ w = \frac{(1+\nu)F_c}{2\pi E} \left[\frac{2(1-\nu)}{R} + \frac{z^2}{R^3} \right] \end{cases} \quad (28)$$

where R denotes the spatial distance between an arbitrary mass point of the elastic semi-infinite space and the force applying position, and r denotes the projection distance along the r_p -axis direction.

Since inconsistent coordinates will bring unnecessary difficulties to subsequent derivation, the coordinate transformation method is employed to deal with this problem. As shown in Table 2, the transformation coefficient matrix is used to transform the elastic mechanics analytical solutions in polar coordinate form into the ones in Cartesian form.

By coordinate transformation, the normal stress field can be formulated as

$$\begin{cases} \sigma_x = \sigma_r \cos^2 \theta + \sigma_\theta \sin^2 \theta \\ \sigma_y = \sigma_r \sin^2 \theta + \sigma_\theta \cos^2 \theta \\ \sigma_z = \sigma_z \end{cases} \quad (29)$$

Substituting Eq. (27) into Eq. (29), yields

$$\begin{cases} \sigma_x = \frac{F_c(1-2\nu)}{2\pi} \left[\frac{r^2 \cos^2 \theta - r^2 \sin^2 \theta}{r^2 R(R^2+z)} - \frac{3zr^2 \cos^2 \theta}{R^5(1-2\nu)} + \frac{zr^2 \sin^2 \theta}{r^2 R^3} \right] \\ \sigma_y = \frac{F_c(1-2\nu)}{2\pi} \left[\frac{r^2 \sin^2 \theta - r^2 \cos^2 \theta}{r^2 R(R^2+z)} - \frac{3zr^2 \sin^2 \theta}{R^5(1-2\nu)} + \frac{zr^2 \cos^2 \theta}{r^2 R^3} \right] \\ \sigma_z = -\frac{3F_c z^3}{2\pi R^5} \end{cases} \quad (30)$$

One of the basic properties of polar coordinates can be formulated as

$$\begin{cases} x = r \cos \theta \\ y = r \sin \theta \\ R = \sqrt{x^2 + y^2 + z^2} \end{cases} \quad (31)$$

Substituting Eq. (31) into Eq. (30), yields

$$\begin{cases} \sigma_x = \frac{F_c(1-2\nu)}{2\pi} \left[\frac{x^2 - y^2}{\sqrt{x^2 + y^2} \sqrt{x^2 + y^2 + z^2} (\sqrt{x^2 + y^2 + z^2} + z)} - \frac{3zx^2}{(x^2 + y^2 + z^2)^{\frac{5}{2}}(1-2\nu)} + \frac{zy^2}{(x^2 + y^2 + z^2)^{\frac{3}{2}}(x^2 + y^2)} \right] \\ \sigma_y = \frac{F_c(1-2\nu)}{2\pi} \left[\frac{y^2 - x^2}{\sqrt{x^2 + y^2} \sqrt{x^2 + y^2 + z^2} (\sqrt{x^2 + y^2 + z^2} + z)} - \frac{3zy^2}{(x^2 + y^2 + z^2)^{\frac{5}{2}}(1-2\nu)} + \frac{zx^2}{(x^2 + y^2 + z^2)^{\frac{3}{2}}(x^2 + y^2)} \right] \\ \sigma_z = -\frac{3F_c z^3}{2\pi (x^2 + y^2 + z^2)^{\frac{5}{2}}} \end{cases} \quad (32)$$

Analogously, the displacement field in Cartesian form can be calculated by

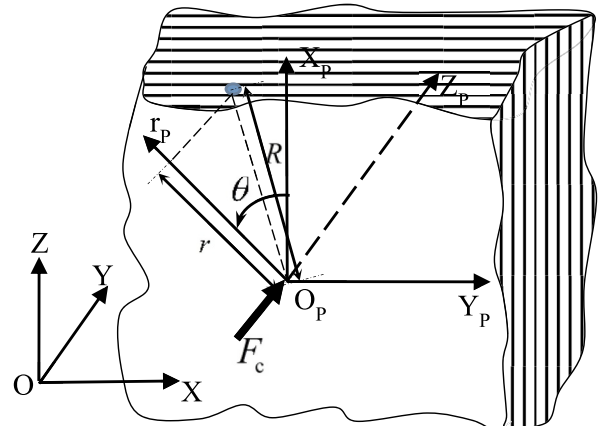


Fig. 9. The elastic semi-infinite space and coordinate transformation.

Table 1
Dimensions of the Span region and material information for Example I.

Symbol	Explanation	Value
L_a	Length of the Span region	64 mm
L_b	Width of the Span region	236 mm
b	Width of the engine block	108 mm
R_b	Radius of the cylinder bore	35 mm
E	Elastic modulus of HT250	140 GPa
ν	Poisson ratio of HT250	0.27

Table 2
Transformation coefficient matrix of polar and local Cartesian coordinate systems.

Coordinate axis	r	θ	Z
X_p	$\cos \theta$	$-\sin \theta$	0
Y_p	$\sin \theta$	$\cos \theta$	0
Z_p	0	0	1

$$\begin{cases} u = \frac{(1+\nu)F_c}{2\pi E} \left[\frac{\sqrt{x^2+y^2}z}{(x^2+y^2+z^2)^{\frac{3}{2}}} - (1-2\nu) \frac{\sqrt{x^2+y^2}}{\sqrt{x^2+y^2+z^2}(\sqrt{x^2+y^2+z^2}+z)} \right] \\ v = \frac{(1+\nu)F_c}{2\pi E} \left[\frac{\sqrt{x^2+y^2}z}{(x^2+y^2+z^2)^{\frac{3}{2}}} - (1-2\nu) \frac{\sqrt{x^2+y^2}}{\sqrt{x^2+y^2+z^2}(\sqrt{x^2+y^2+z^2}+z)} \right] \\ w = \frac{(1+\nu)F_c}{2\pi E} \left[\frac{2(1-\nu)}{\sqrt{x^2+y^2+z^2}} + \frac{z^2}{(x^2+y^2+z^2)^{\frac{3}{2}}} \right] \end{cases} \quad (33)$$

Denoting the coordinates of an arbitrary mass point of the workpiece w.r.t. the local and global CCSs as $[M] = (x, y, z)^T$ and $[M'] = (x', y', z')^T$ respectively, by homogeneous coordinate transformation, it can be derived that

$$[M] = \begin{bmatrix} 0 & 0 & 1 \\ 1 & 0 & 0 \\ 0 & 1 & 0 \end{bmatrix} [M'] + \begin{bmatrix} -z_c \\ -x_c \\ -y_c \end{bmatrix} \quad (34)$$

which can be rewritten as

$$\begin{bmatrix} x \\ y \\ z \end{bmatrix} = \begin{bmatrix} z' - z_c \\ x' - x_c \\ y' - y_c \end{bmatrix} \quad (35)$$

where (x_c, y_c, z_c) denotes the coordinates of the force applying point w.r.t. the global CCS.

Note that the assumption about the elastic semi-infinite space is not entirely suitable for the Pier region because there are two finite boundaries, the top and bottom surfaces. The elastic mechanics based analytical solution to deformation of top surface, which is to be machined in the following processes, will be distort due to the finite boundaries. To overcome this disadvantage, a virtual plane method is proposed. As shown in Fig. 10, the virtual plane S_λ is defined by the parameter λ ($0 < \lambda < H - z'$) that refers to the distance between the top surface and the virtual plane.

Since this paper is focused on the machining quality improvement of the top surface, calculation accuracy of the bottom surface is relatively non-critical. Moreover, the other three boundaries are all sections, consisting of two Pier-Span sections and one Pier-Bridge section. Therefore, the part of a Pier region below S_λ can be viewed as an elastic semi-infinite space, while the rest part can be viewed as an elastic plate loaded with an arbitrary load from the virtual plane. Consequently, the stress and displacement field below S_λ can be calculated by Eq. (32) and

Eq. (33) respectively. Taking the stress on the virtual plane as the input load function, the mid-surface deflection of the part above S_λ can be calculated by Eq. (22).

Example II. An example is given in order to illustrate the proposed approach to calculating the fixturing induced deformation of the Pier region before the machining process. A concentrated clamping force F_c known as 130 N, is perpendicularly exerted on a point of the flank of a Pier region, namely, $P_p(86, 0, 195)$ w.r.t. the global CCS $OXYZ$. A local CCS $O_p X_p Y_p Z_p$ is established and P_p is taken as the origin. According to Eq. (35), the global coordinates (x', y', z') of an arbitrary mass point in the Pier region can be transformed into the local one by $x = z' - 195$, $y = x' - 86$, and $z = y'$. Since the Boussinesq condition is satisfied if and only if the mass point is below the virtual plane S_λ , the calculation accuracy is dependent on the value of the parameter λ . The height of the VSS workpiece is known as $H = 236$ mm, therefore λ should be less than $H - z' = 41$ mm to ensure S_λ is beyond the force applying position, i.e. λ ranges from 0 to 41 mm. To determine an appropriate value of λ , a sensitivity analysis is implemented based on the comparison between the proposed analytical solutions of the displacement field with different values of λ and corresponding results given by FEM. As shown in Fig. 11, the parameter Delta denotes the absolute percentage of the deviation between the proposed analytical solutions and the FEM-based numerical solutions. It is found that as λ grows from 0, Delta decreases sharply at first, and then enters the trough when λ reaches about 10 mm, and finally increases gently till λ approached to the upper bound, for both the maximum and the average deformation.

Therefore, λ is set to 11 mm and the deviation from the conventional FEM-based numerical results is within 10%, which is acceptable in this paper. By Eq. (32), the stress field of the Pier region below S_λ can be calculated, which becomes the load input of Eq. (22) so as to calculate the deflection of the Pier region above S_λ , and finally the displacement field of the top surface is obtained, shown as Fig. 12. The maximum deformation induced by the clamping force in this example is 0.016 mm.

2.2.4. Bridge region

As the most representative instance for the variable stiffness structure, the Bridge region has the following properties. Firstly, there is no external load directly exerted on the Bridge region and therefore the deformation is depended on loading condition on the Pier-Bridge section. Secondly, loading condition on the Pier-Bridge section is equal in magnitude and opposite in direction to the stress field obtained in

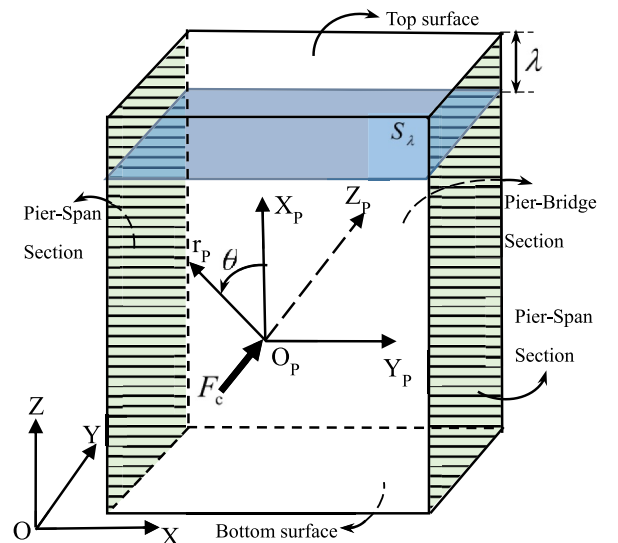


Fig. 10. Elasticity analysis of the Pier region using virtual plane.

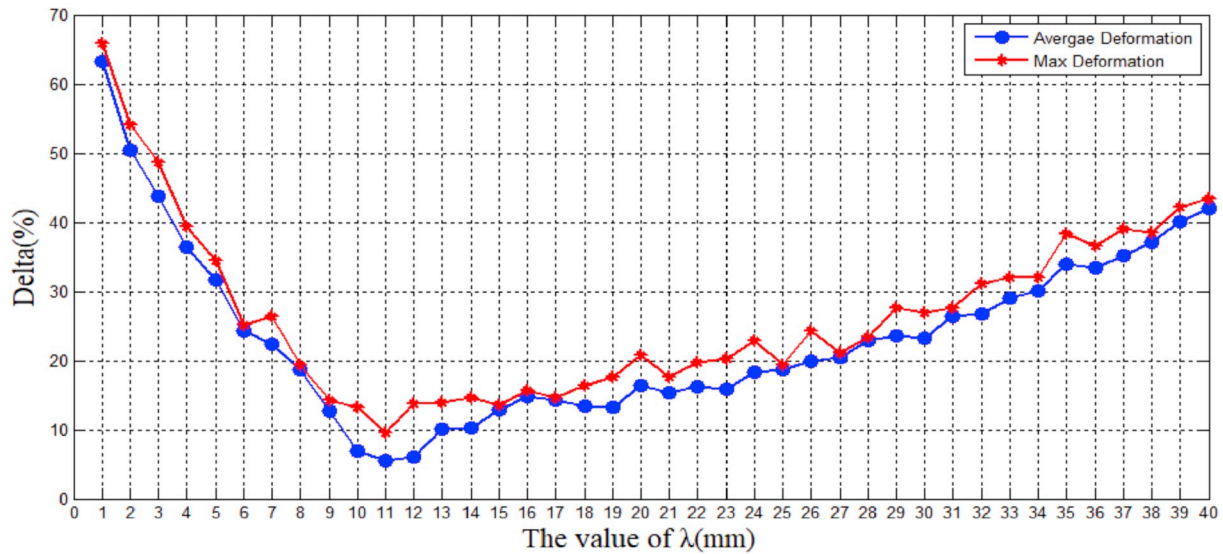


Fig. 11. Sensitivity analysis of the value of λ .

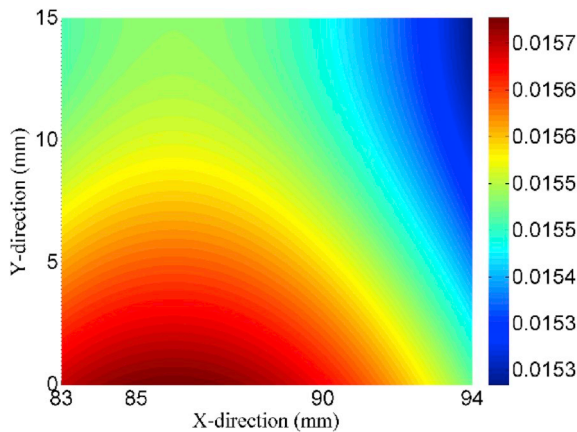


Fig. 12. Displacement field of the top surface of a Pier region with a perpendicular concentrated force loaded on its flank.

elasticity analysis of Span and Pier regions. Last but not least, analogous to the equivalent treatment of the Span region, the Bridge region can be deemed as a semi-infinite elastic sheet with variable stiffness.

For a semi-infinite elastic sheet with unit width (see Fig. 13), in two-dimensional polar coordinate form, the basic equations for elasticity analysis given by Ref. [37] are shown as follows.

The static equilibrium equations are

$$\begin{cases} \frac{\partial \sigma_r}{r} + \frac{\partial \tau_{r\theta}}{r\partial\theta} + \frac{\sigma_r - \sigma_\theta}{r} = 0 \\ \frac{\partial \sigma_\theta}{r\partial\theta} + \frac{\partial \tau_{r\theta}}{\partial r} + \frac{2\tau_{r\theta}}{r} = 0 \end{cases} \quad (36)$$

The strain-displacement relationship can be formulated as

$$\begin{cases} \epsilon_r = \frac{\partial u}{\partial r} \\ \epsilon_\theta = \frac{\partial v}{r\partial\theta} + \frac{u}{r} \\ \gamma_{r\theta} = \frac{\partial v}{\partial r} + \frac{\partial u}{r\partial\theta} - \frac{v}{r} \end{cases} \quad (37)$$

The elastic constitutive equations are formulated as

$$\begin{cases} \epsilon_r = \frac{1}{E}(\sigma_r - \nu\sigma_\theta) \\ \epsilon_\theta = \frac{1}{E}(\sigma_\theta - \nu\sigma_r) \\ \gamma_{r\theta} = \frac{1}{G}\tau_{r\theta} \end{cases} \quad (38)$$

The stress components can be expressed by stress function ϕ as follows.

$$\begin{cases} \sigma_r = \frac{\partial^2 \phi}{r^2 \partial r^2} + \frac{\partial^2 \phi}{r^2 \partial \theta^2} \\ \sigma_\theta = \frac{\partial^2 \phi}{\partial r^2} \\ \tau_{r\theta} = \frac{\partial \phi}{r^2 \partial \theta} - \frac{\partial^2 \phi}{r \partial r \partial \theta} \end{cases} \quad (39)$$

Given that $\phi = -\frac{P}{\pi} r \theta \sin \theta$, based on Eq. (39), a basic solution to stress field can be derived as

$$\begin{cases} \sigma_r = -\frac{2P \cos \theta}{\pi r} \\ \sigma_\theta = \tau_{r\theta} = 0 \end{cases} \quad (40)$$

where P is the uniformly distributed load perpendicularly exerted on the straight boundary of an elastic sheet with unit width.

This basic solution satisfies Eq. (36), and it satisfies the boundary conditions of the straight boundary as well. That is, there is no other external load on the straight boundary except for $r = 0$, which can be formulated as

$$\begin{cases} \sigma_r|_{\theta=\frac{\pi}{2}, r \neq 0} = 0 \\ \sigma_\theta|_{\theta=\frac{\pi}{2}} = \tau_{r\theta}|_{\theta=\frac{\pi}{2}} = 0 \end{cases} \quad (41)$$

Taking the load applying position as the center, for a cylindrical surface with an arbitrary radius denoted by r , the resultant force of the cylindrical surface is balanced by P . That is,

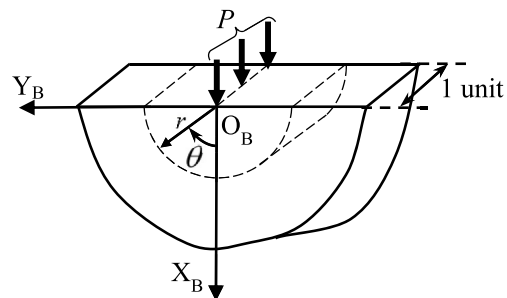


Fig. 13. Elasticity analysis of a semi-infinite elastic sheet under the uniformly distributed load exerted on its straight boundary in two-dimensional polar coordinate form.

$$2 \int_0^{\frac{\pi}{2}} \sigma_r r \cos \theta d\theta = -P \tag{42}$$

It can be proved that the basic stress solution given by Eq. (40) satisfies this constraint as well. Hence, Eq. (40) is the exact stress solution to elasticity analysis of the semi-infinite elastic sheet under the uniformly distributed load exerted on its straight boundary. And the deformation solution can be calculated by

$$\begin{cases} u = \frac{P}{\pi E} [2(\ln d_B - \ln r) \cos \theta - (1 - \nu) \theta \sin \theta] \\ v = \frac{P}{\pi E} [2(\nu + \ln r - \ln d_B) \sin \theta + (1 - \nu)(\sin \theta - \theta \cos \theta)] \end{cases} \tag{43}$$

where d_B denotes the minimum distance between the origin and the mass point of X-axis whose vertical displacement is equal to 0. The detailed derivation can be found in Appendix A.

As for the Bridge region (see Fig. 14), however, due to stress concentration and different applying positions of clamping forces, there is a strong possibility that stress load exerted on the Pier-Bridge section is non-coplanar with the middle surface of the Bridge region. According to the Saint-Venant theorem [37], the stress load can be approximate to a biased concentrated force P , and then equivalent to a parallel concentrated force P' and a corresponding balanced torque T composed of P and P'' . The magnitude of P' is same with that of P and P' is coplanar with the middle surface of the Bridge region. Denoting the bias of P as d_p , yields $T = Pd_p$.

The analytical solutions given by Eq. (40) and Eq. (43) are both two-dimensional and feasible only under the assumption that the sheet thickness is equal to 1 unit, which is not applicable for the Bridge region. The thickness of the Bridge region $l(x)$ is actually a continuous function of variable x , formulated as

$$l(x) = \frac{d_2}{2} - \sqrt{R_b^2 - \left(\frac{d_3}{2} - x\right)^2} \tag{44}$$

Thus the effect of the variable stiffness should be considered and the previous solutions need to be modified and extended.

Induced by the torque T , the deflection of the mid-surface can be calculated by

$$w = \sqrt{R_c^2 - \left(\frac{d_3}{2} - x\right)^2} - \sqrt{R_c^2 - \left(\frac{d_3}{2}\right)^2} \tag{45}$$

where R_c denotes the curvature radius and is given by $R_c = \frac{E(l(x))^3}{12Pd_p}$.

It can be seen that the horizontal section area of the Bridge region varies with the variable x , whereas the longitudinal section area keeps constant. Therefore, the actual compressive stiffness along the X_B -axis and Y_B -axis the can be formulated as $K_x = EHL(x)$ and $K_y = EA_B$ respectively, where A_B is a known constant referring to the area of the top surface of Bridge region. In order to conform to the assumption of elastic sheet with unit width, i.e., $K_x = E_x H$ and $K_y = E_y d_3$, two modified elastic moduli, $E_x = El(x)$ and $E_y = \frac{EA_B}{d_3}$, are proposed. Thus, by modifying Eq. (43) and integrating with Eq. (45), the three-dimensional displacement field of the Bridge region can be calculated by

$$\begin{cases} u = \frac{P}{\pi El(x)} [2(\ln d_B - \ln r) \cos \theta - (1 - \nu) \theta \sin \theta] \\ v = \frac{Pd_3}{\pi EA_B} [2(\nu + \ln r - \ln d_B) \sin \theta + (1 - \nu)(\sin \theta - \theta \cos \theta)] \\ w = \sqrt{R_c^2 - \left(\frac{d_3}{2} - x\right)^2} - \sqrt{R_c^2 - \left(\frac{d_3}{2}\right)^2} \end{cases} \tag{46}$$

Example III. . An example is given in order to illustrate the proposed approach to calculating the fixturing induced deformation of the Bridge Span region before the machining process. The analytical solutions to stress fields of the Span and Pier regions are superposed as the load input of the elasticity analysis. Due to the stress concentration on the edges of the Pier-Bridge section (see Fig. 15), according to Eq. (8), the biased vertical concentrated force P can be calculated

by $P = K_{sc} \frac{\iint \sigma_x dydz}{Hl(0)}$. The bias of P is known as $d_p = 0.5l(0)$.

Therefore, given the stress concentration coefficient K_{sc} equals to 3.2, the displacement field of the top surface of the Bridge can be calculated by Eq. (46), as shown in Fig. 16. The maximum deformation induced by the clamping force in this example is 0.022 mm.

2.3. Fixture layout optimization model

After completion of elasticity analysis of three types of regions, the fixturing induced deformation of the VSS workpiece is available, which provides access to possibility of effective and efficient fitness calculation for fixture layout optimization. For a VSS workpiece, a poor choice of fixture layout can lead to undesirable deformation during fixturing, consequently resulting in low dimensional or form accuracy after machining. Hence, it is necessary to propose an appropriate model for fixture layout optimization.

2.3.1. Objective and constraints

The ultimate goal of this study is to improve the quality of the machined surface of the workpiece. Due to the elastic deformation recovery during fixture unloading after machining (see Fig. 17), the fixturing induced deformation effects mainly on the form accuracy, especially for the flatness of the machined surface.

It can be seen that the larger the maximum fixturing induced deformation is, the poorer the final surface quality will be. In other words, the main objective of this optimization model is to minimize the maximum fixturing induced deformation, so that the global flatness of the top surface after face milling is improved. Therefore, the objective function is given as

$$\min S(\mathbf{X}) \tag{47}$$

where $\mathbf{X} = [L_1, L_2, \dots, L_6, C_1, C_2, \dots, C_6]^T$ denotes the fixture layout with a 3-2-1 locating principle, composed of six positions of locators and six positions of clamps. Once given a certain set of machining parameters such as axial cutting depth and feed per tooth, the corresponding optimal magnitudes of clamping forces are determined by \mathbf{X} , thus $S(\mathbf{X})$ is a function merely involving \mathbf{X} , referring to the maximum absolute value of displacement of the top surface.

Important constraints in fixture layout design are summarized as

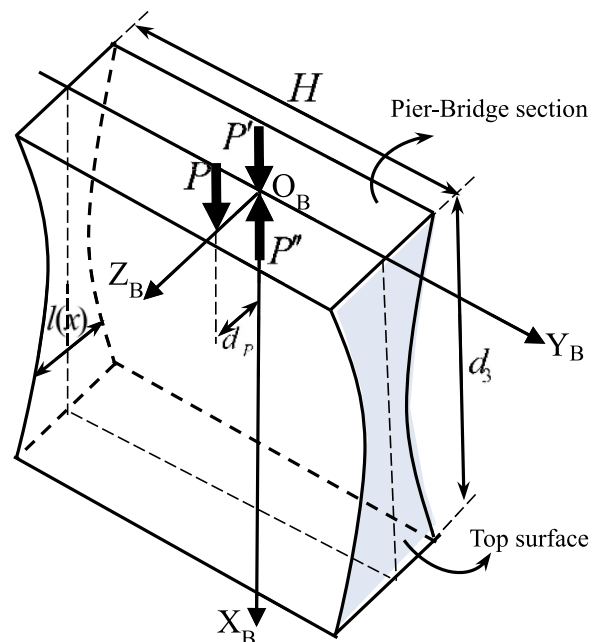


Fig. 14. Elasticity analysis of the Bridge region with the Saint-Venant theorem.

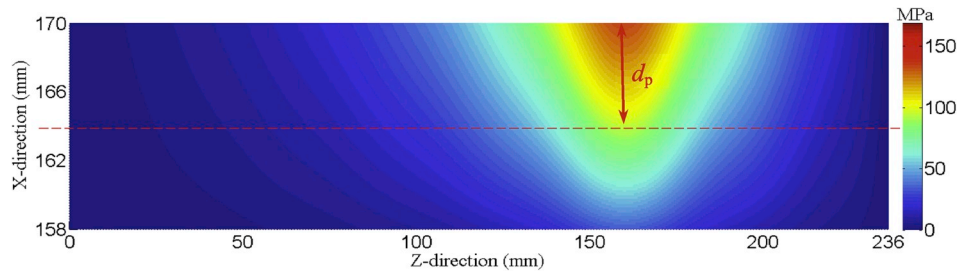


Fig. 15. The stress concentration on the edges of the Pier-Bridge section.

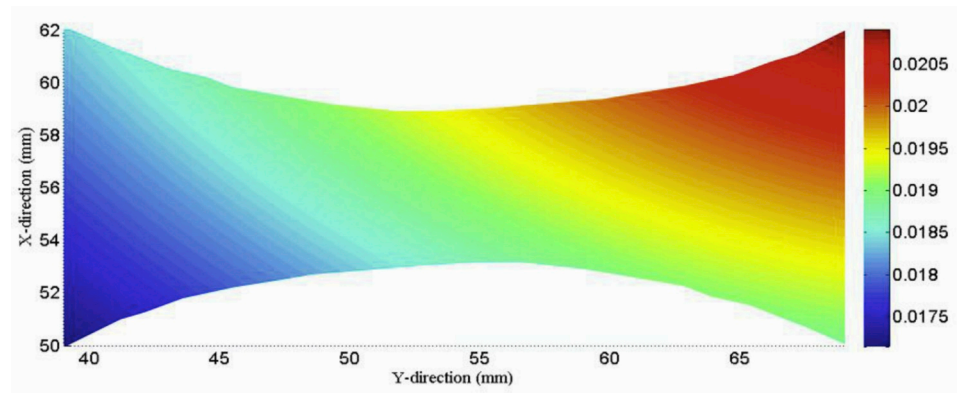


Fig. 16. Displacement field of the top surface of a Bridge region with the stress concentration on the edges of the Pier-Bridge section.

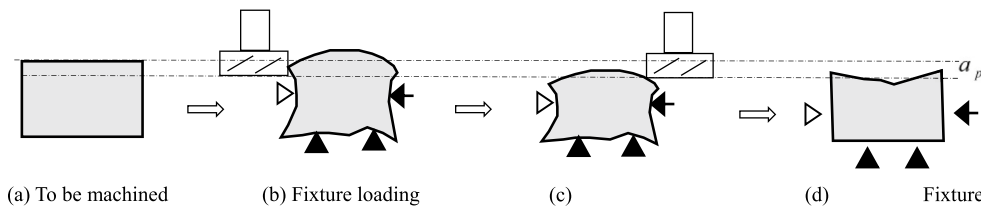


Fig. 17. The effect of elastic deformation recovery on final form accuracy.

follows.

Constraint 1: The fixture elements should not interfere with the desired tool path, i.e., the proposed fixture layout should not hamper features being machined. Thus the number of locator-clamp pairs perpendicular to the tool path should be as few as possible, which is set to 1 in this study.

Constraint 2: There should be corresponding faces or features on the workpiece, meeting a certain level of quality requirements for fixture elements to contact with them. It means that not all positions on the workpiece are suitable for supporting, locating, or clamping, which has significantly reduced the feasible domain of this problem.

Constraint 3: The position and orientation of the workpiece w.r.t. expected datum planes should be precisely specified by the fixture layout, the degree of freedom of the workpiece being completely constrained. And of course, over-locating should be avoided as well.

2.3.2. Computation rules for GA

Since the optimization model is nonlinear and complex, GA is employed to solve it. According to the general procedures of GA, several computation rules are proposed as follows.

Rule 1: Fitness computation. Since excessive deformation is undesirable and meaningless to fixture layout optimization, a threshold of the maximum deformation denoted by S_0 is proposed. Once the maximum deformation exceeds the threshold, fitness is immediately set to 0. For a certain fixture layout, the fitness can be calculated by

$$fitness = \begin{cases} \alpha_S(S_0 - S) & S < S_0 \\ 0 & \text{else} \end{cases} \quad (48)$$

where α_S is the fitness weight function of S , providing nonlinear variation for fitness weight if needed, and it can be set to a constant as well.

Rule 2: Selection, crossover and mutation. In order to increase robustness of the method, a roulette-wheel selection algorithm [57] is implemented. Two chromosomes are randomly selected based on the cumulative distribution function of fitness, instead of simply selected by maximum fitness, as the objects for crossover and



Fig. 18. A four-cylinder block of B12 engine.

Table 3
The predefined parameters in the case study.

Symbol	Explanation	Value
a	Length of the engine block	326.5 mm
b	Width of the engine block	108 mm
H	Height of the engine block	236 mm
d_1	Distance from the first center line to the front face	51 mm
d_2	Distance between two adjacent center line	75.5 mm
d_3	Length of the Bridge region	30 mm
R_b	Radius of the cylinder bore	35 mm
A_B	Top surface area of the Bridge region	47.37 mm ²
ζ_R	Safety coefficient for clamping force	1.7
K_{sc}	Stress concentration coefficient	3.2
λ	Distance between the virtual plane to the top surface	11 mm
S_0	Threshold of the maximum deformation	0.03 mm
α_S	Fitness weight function	10 ⁴
p_c	Crossover probability	0.9
p_m	Mutation probability	0.1–0.3
g_c	Convergence generation	2000

Table 4
The experiment design of different machining parameters.

Number	f_z (mm)	a_p (mm)	N
1	0.1	0.1	6
2	0.12	0.15	8
3	0.14	0.2	10
4	0.16	0.12	8
5	0.18	0.17	10
6	0.2	0.22	6
7	0.22	0.08	10
8	0.24	0.12	6
9	0.26	0.18	8

mutation. The crossover probability is set to a constant, whereas the mutation probability is a piecewise increasing function of generations, so as to improve the ability to escape from the local optimal solutions.

Rule 3: Stopping criteria. The iteration will be stopped if and only if the maximum fitness is continuously maintained at a certain level for a given number of generations, and then the GA employed in this study is deemed to converge to the global optimal solution.

3. Case study

In this case, a four-cylinder block of B12 engine (see Fig. 18) is used to validate the performance of the proposed approach on fixturing scheme optimization of VSS workpieces for surface quality improvement. In the assembly process, the top surface of cylinder block contacts

with one side of the gasket directly, and the other side of the gasket contacts with the cylinder head. Thus, the top surface quality, especially for the form accuracy, will influence the sealing performance and reliability of the engine.

The top surface is finished by the face milling process with a 3-2-1 locating principle. However, the current fixturing scheme relies merely on the experience of the engineers, which has a considerable space to improve. Therefore, this case is focused on form accuracy improvement of the top surface in the face milling process by fixturing scheme optimization.

The predefined parameters used in this case are shown in Table 3.

3.1. Milling force measurement

In order to obtain the undetermined coefficients A_q and B_q of the static cutting force model by Eq. (4), an experiment design consisting of nine sets of different machining parameters is implemented. And the designed machining parameters are given by Table 4 in detail. Since the spindle speed V_s is not explicitly contained in the proposed static cutting force model, it is fixed to 400 rounds per minute (rpm) in this case.

The experiment of milling force measurement is conducted within a DMG–HSC–75 computer numerical control (CNC) machining center (see Fig. 19 (a)). With nine sets of different machining parameters, a series of face milling processes are performed on a quarter of the B12 engine block. The milling force components are measured by 9027C type Kistler three-component dynamometer. Specifically, the milling force signal is detected by the acceleration sensors embedded in the vise, and then transmitted by the sensor cable (see Fig. 19 (b)), and at last amplified and collected by the signal acquisition device (see Fig. 19 (c)). The sampling period is 30 s.

As shown in Fig. 20, the raw signal is processed by a 2-order low pass filter and intercepted by 8 s as the stable milling stage. The lower edge frequency of the filter is 50 Hz while the higher one is 100 Hz.

It can be seen that there are two peaks and one trough in the waveform of each signal segment, indicating that the milling force magnitude rises when the milling cutter contacts with the Pier and Bridge regions, and declines when the milling cutter contacts with the Span regions. The fluctuation of the milling force magnitude conforms to the variation of radial cutting depth, which is determined by the geometric features of the VSS workpiece. In terms of the quarter of the B12 engine block used in this experiment, the major geometric feature is the cylinder bore. Therefore, the measurement results are reasonable.

By calculating the average magnitude of milling forces along each coordinate axis for different machining parameters, and least square fitting of Eq. (4), the undetermined coefficients of the static cutting force model are available, as shown in Table 5.

This experiment of milling force measurement has provided an access to calculate the undetermined coefficients of the static cutting force

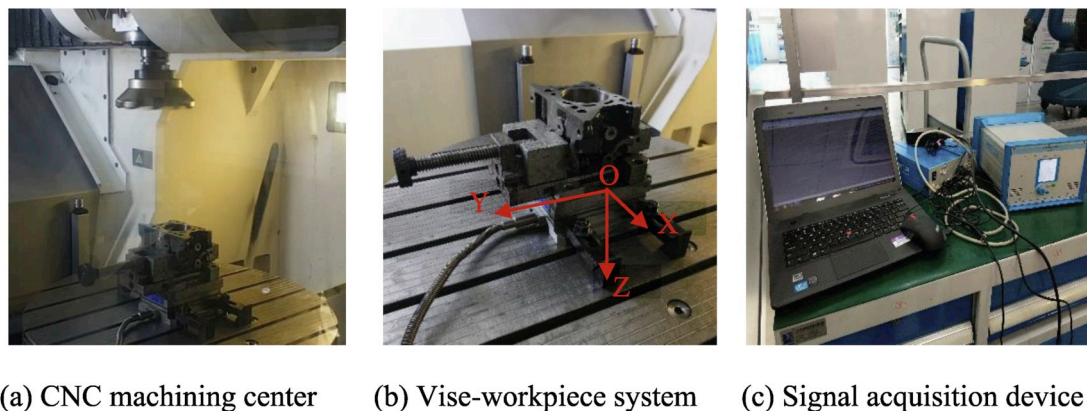


Fig. 19. Experimental setup of milling force measurement.



Fig. 20. The filtered milling force signal in the stable stage.

Table 5
Undetermined coefficients of static cutting force model with 400 rpm spindle speed.

Coefficients	A_x	A_y	A_z	B_x	B_y	B_z
Value	0.2413	0.3341	0.5113	6.5408	6.8744	7.1703

Table 6
Material properties of gray cast iron HT250.

Density	Elastic modulus	Poisson ratio
7200 kg/m ³	140 GPa	0.27

model, so as to determine the optimal magnitudes of corresponding clamping forces, which will be the load input for elasticity analysis. The B12 engine block is made of gray cast iron HT250, and its material properties are given by Table 6, which will be used in both elasticity analysis and FEM simulation.

3.2. Optimized fixturing scheme verification

3.2.1. Initial fixturing scheme

Limited to the actual physical configuration of the B12 engine block, the positions of locators and clamps are not arbitrary indeed, as mentioned in the second constrain of fixture layout design. For the primary locating datum plane and its opposite plane, seven candidate positions

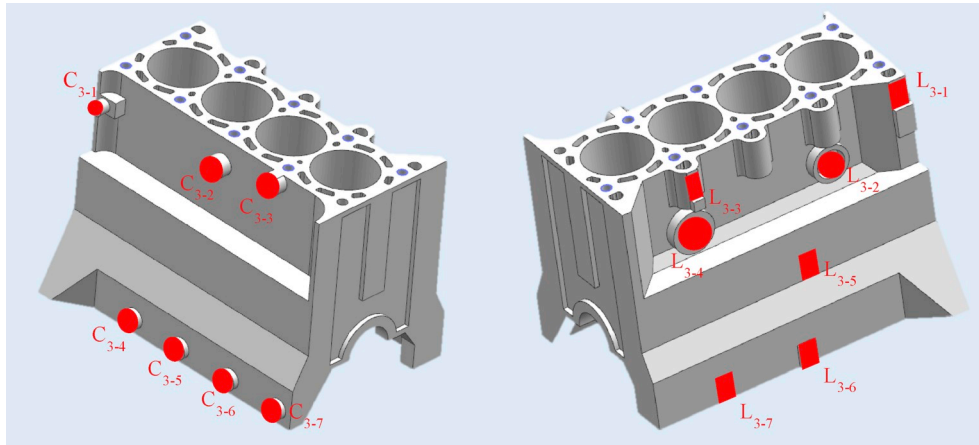


Fig. 21. Candidate positions for locating and clamping on the primary locating datum plane and its opposite plane.

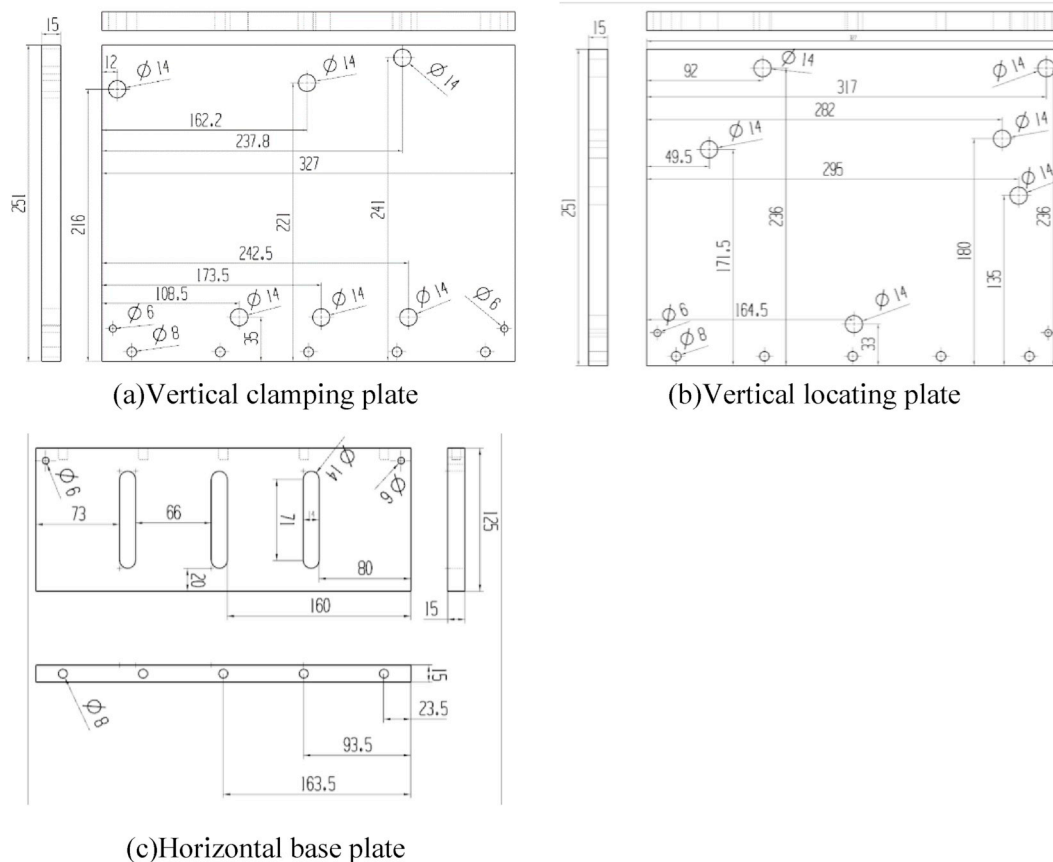


Fig. 22. Three views of the combined L-plates.

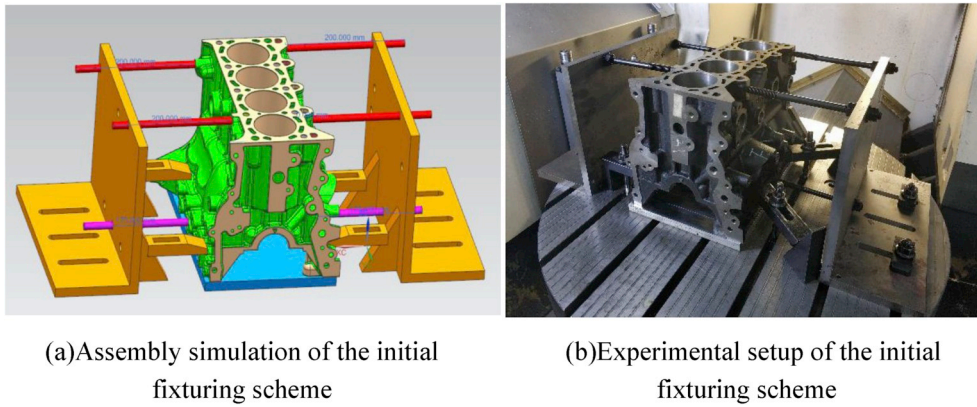


Fig. 23. The initial fixturing scheme.

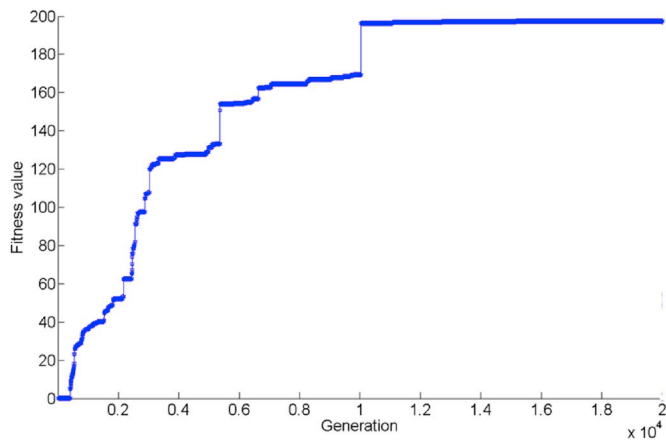


Fig. 24. The trend of the maximum fitness value with increasing iterations.

are provided for locating (from L₃₋₁ to L₃₋₇) and clamping (from C₃₋₁ to C₃₋₇) respectively (see Fig. 21). Three of the candidate locating positions and three or four of the candidate clamping positions should be picked out as a fixture layout.

The currently used fixturing scheme in actual production, termed as the initial fixturing scheme, is designed mainly based on engineering experience. The positions of L₃₋₁, L₃₋₃, L₃₋₆, C₃₋₁, C₃₋₃, and C₃₋₅ are arranged for locating and clamping respectively. And the initial magnitudes of clamping forces are given as 130 N, 210 N, and 235 N for C₃₋₁, C₃₋₃, and C₃₋₅ respectively.

A set of combined L-type plates (see Fig. 22) is designed to realize the locating and clamping for the B12 engine block. There are two



Fig. 26. Clamping force exertion by the torque wrench.

Table 7
Pre-tightening coefficient for different contact conditions of friction surfaces.

K_1	Lubrication	No lubrication
Finishing surface	0.01	0.012
Roughing surface	0.013–0.015	0.018–0.026
Oxidized surface	0.02	0.024
Galvanized surface	0.018	0.022

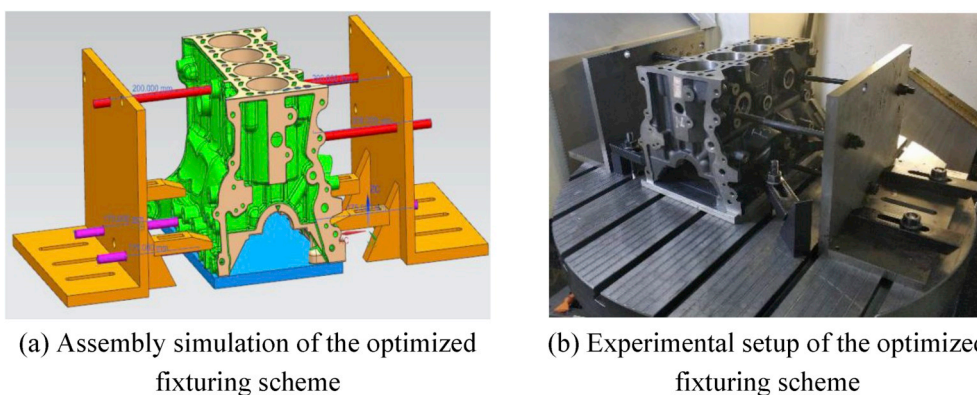


Fig. 25. The optimized fixturing scheme.

Table 8
Pre-tightening torque needed for different fixturing scheme (N·m).

Clamping position	Initial fixturing scheme	Optimized fixturing scheme
C ₃₋₁	36	0
C ₃₋₂	0	41
C ₃₋₃	59	0
C ₃₋₄	0	27
C ₃₋₅	66	0
C ₃₋₆	0	34
C ₃₋₆	0	0



Fig. 27. Machining process within the CNC machining center.

vertical plates, one for clamping and the other one for locating. Several holes with specific locations and sizes are drilled through both of the two vertical plates, so that the bolts can be arranged to locate and exert clamping forces on the corresponding positions of the engine block, and the vertical plates can be combined with the horizontal base plates by screws as well. The horizontal base plates are fixed on the worktable to keep the combined L-type plates stable during fixturing and machining.

The assembly drawing generated by Unigraphics NX 10.0 and the experimental setup of the initial fixturing scheme are shown as Fig. 23.

3.2.2. Optimized fixturing scheme

For a certain fixture layout, the optimal magnitudes of clamping forces can be obtained by Eq. (4), based on the results of the milling force measurement as given by Table 5. Taking the optimized clamping forces as the load input, the fixturing induced deformation of Span regions, Pier regions and Bridge regions can be calculated by Eq. (26), Eq. (33) and Eq. (46) respectively. And then they are superposed to form the analytical solution of total deformation induced by fixturing. By solving the optimization model aimed at minimizing the maximum fixturing induced deformation with GA, the optimal fixturing scheme is obtained. The convergence of GA is shown in Fig. 24.

It can be seen that there is a staged increase in maximum fitness within the generations from 1 to 1600. And eventually the stopping criteria is satisfied due to the maximum fitness has been continuously maintained at 196 for over 2000 generations, which means that the iteration process has converged to the global optimal solution.

The theoretical optimal solution obtained from GA is to locate on the positions of L₃₋₂, L₃₋₄ and L₃₋₆, and to clamp on the positions of C₃₋₂, C₃₋₄, and C₃₋₆ with 145 N, 95 N, and 120 N respectively. And the maximum fixturing induced deformation of the top surface is 0.0172 mm. The assembly drawing and the experimental setup of the optimized fixturing scheme are shown as Fig. 25.

To exert the clamping force with the exact magnitude, a torque wrench (see Fig. 26) is used during fixturing, whose range is up to 200

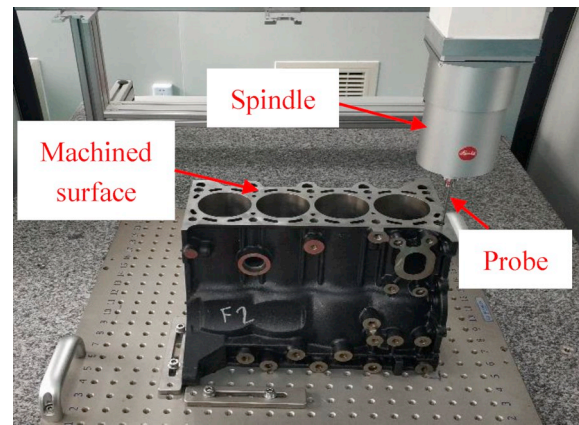


Fig. 28. Machined surface quality measurement by the CMM system.

Nm. The transform relationship between the pre-tightening torque g_c exerted on the bolts by the wrench and the clamping force F_c exerted on the engine block by the bolts [58] can be formulated as

$$M_t = K_t F_c D_b \quad (49)$$

where K_t denotes the pre-tightening coefficient, varying with different contact conditions of friction surfaces given in Table 7, while D_b denotes the diameter of the bolt.

In this case, the bolt diameter D_b is uniformly equals to 14 mm and K_t is set to 0.02. Therefore, the pre-tightening torques needed for the initial fixturing scheme and the optimized fixturing scheme are given by Table 8. Note that the rounding induced error is in an acceptable range due to the minimum precision limit of the torque wrench.

3.2.3. Verification

3.2.3.1. Experimental verification. A machining experiment is conducted to verify the effectiveness of the proposed approach. Face milling operations are performed on two engine blocks within the DMG–HSC–75 CNC machining center (see Fig. 27), using a disc milling cutter with a diameter of 160 mm and 8 cubic boron nitride (CBN) teeth. The cutting speed is set to 64000 mm/min, the depth of cut is set to 0.15 mm, and the feed rate is set to 320 mm/min. Quaker 370 KLG cutting fluid is used. The machining process is under closely supervised conditions to ensure that no anomalous problems occur.

The LEITZ-PMM-XI coordinate measurement machine (CMM) system (see Fig. 28) is used to measure the flatness of the top surface after milling. For each engine block, 50 randomly selected points on the top surface are measured by the CMM probe. The measured height of the sampling points is shown in Fig. 29.

After coordinate transformation, the flatness of the milled top surface is obtained by the least square method. With the initial fixturing scheme, the flatness of the milled top surface is 0.0254 mm, whereas that with the optimized scheme is 0.0231 mm. The calculation result shows that the proposed approach has improved the flatness by nearly 9.1%.

The detail of comparison between the initial scheme and the optimized scheme is given by Table 9. There are three evaluating indicators, the maximum fixturing induced deformation, the flatness of the machined surface and the computation cost. It can be seen that the proposed approach can improve both the maximum fixturing induced deformation and the quality of the machined surface. And the efficiency of the proposed approach is validated because its computation cost is acceptable.

3.2.3.2. Simulation verification. In order to further validate the effectiveness of the proposed approach, the dynamic explicit FEM [59] is employed to simulate the face milling process on the top surface of the B12 engine block through the software ABAQUS/CAE

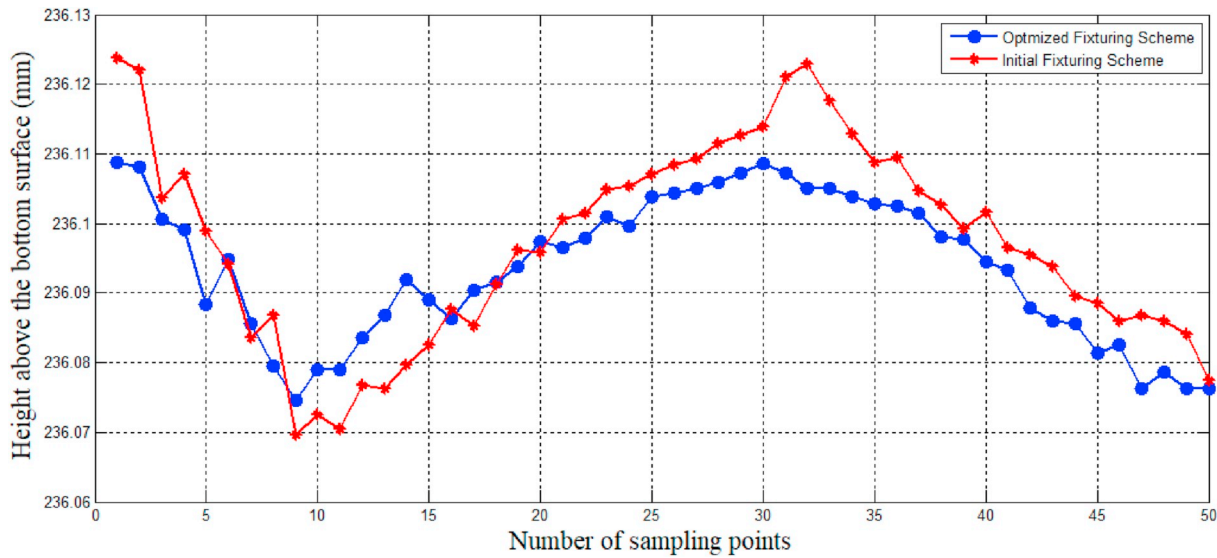


Fig. 29. The measured height of the sampling points.

Table 9
Comparison between the conventional method and the proposed approach.

Evaluating indicators	Initial scheme	Optimized scheme	Improved
Max. fixturing induced deformation	0.0201 mm	0.0172 mm	14.4%
Flatness of the machined surface	0.0254 mm	0.0231 mm	9.1%
Computation cost	0.1 h	0.5 h	Acceptable

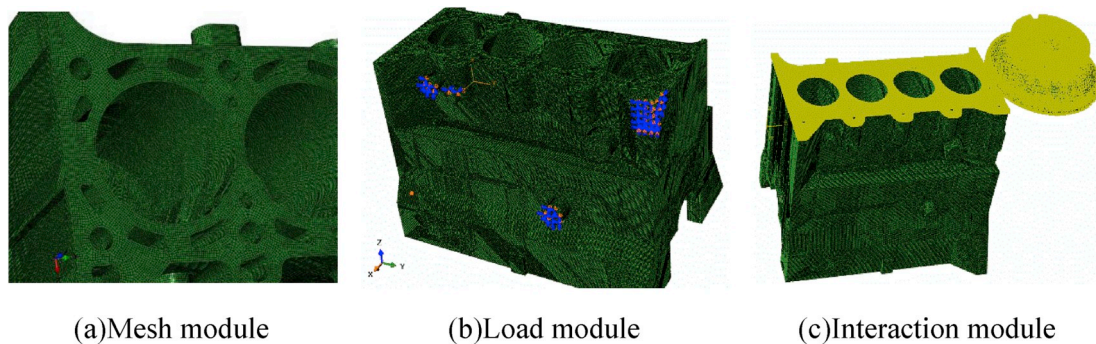


Fig. 30. Main modules of the dynamic explicit FEM.

6.14–1. Main modules of the simulation are shown in Fig. 30.

In the mesh module, the three-dimensional solid element is used for discretization. The total number of nodes is 1887415, while the total number of elements is 4264337, consisting of 1168234 linear hexahedral elements of type C3D8 and 3096103 linear tetrahedral elements of type C3D4. High quality of the mesh ensures the convergence and accuracy of the simulation. In the load module, boundary conditions and clamping loads are exerted to the FEM model. All the input parameters are set as the same as the real machining experiment. And in the interaction module, the interaction properties, especially for the mechanical properties between the tool and the top surface of the engine block are defined. Specifically, for the tangential behavior, the friction formulation is set to Penalty, while for the normal behavior, the pressure overclosure is set to Hard Contact.

The visualization results of the milled top surface of engine block are shown as Fig. 31.

The only difference between these two simulation cases is the fixturing scheme. The displacement field nephogram can be extracted to calculate the flatness of the milled top surface, and it is found that the

final quality of the machined surface is improved by around 11.2% when the proposed fixturing scheme is implemented. The simulation results are conformed to those of the real machining experiment, demonstrating the effectiveness of the proposed approach in surface quality improvement.

4. Conclusion

This paper has developed a systematical approach for fixturing scheme optimization of VSS workpieces for surface quality improvement. The static cutting model is developed to calculate the minimum magnitudes of clamping forces needed to maintain the static equilibrium of the fixture-workpiece system during machining processes. The core model of the proposed approach is derived based on elastic mechanics, instead of the commonly used FEM. By applying a novel division strategy, a typical VSS workpiece are divided into three types of regions according to the geometric features. The analytical solutions of deformation and stress fields of each kind of regions are given, which are relatively straightforward and meaningful, comparing with the

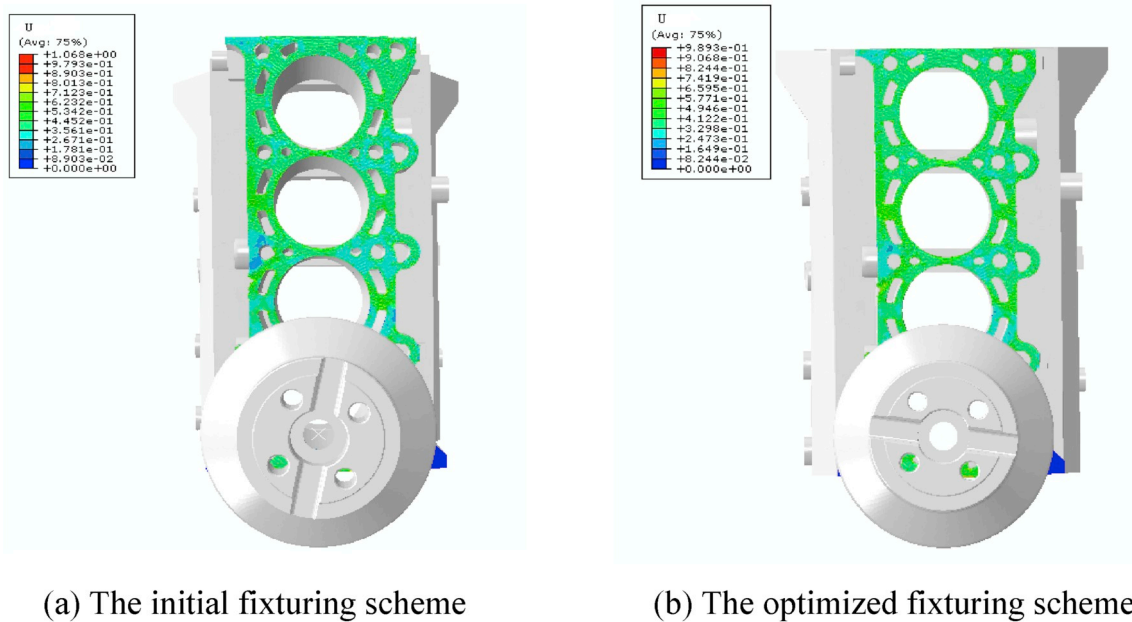


Fig. 31. Dynamic explicit FEM simulation of face milling with different fixturing schemes.

numerical ones. In addition, the analytical solutions make it possible to solve the optimization model by an iterative algorithm efficiently. At last, a case study of a four-cylinder B12 engine block is implemented to verify the performance of the proposed approach. The theoretical optimal fixturing scheme has been compared with the initial one, demonstrating an improvement of the machined surface flatness by around 9.1%.

The practical contribution of these models proposed by this paper lies in providing an analytical approach to optimize the fixturing scheme for face milling and other machining methods suitable for a 3-2-1 locating principle. The optimization process is much more efficient compared with the time-consuming FEM-based numerical methods, which is a significant advantage for practical manufacturing. Besides, the optimal fixturing scheme is quite effective to improve the final quality of the machined surface.

For future work, there are three main aspects worthy of further study. Firstly, the elasticity analysis model could be extended for other VSS workpieces with more complex geometric features, which calls for better mechanics knowledge and richer mathematical skills. Of note is

that the cost of algorithm development and the computation time saving should be balanced. Secondly, in order to obtain a better physical insight of the fixture-workpiece system during machining process, the analytical relationship between the clamping forces and the cutting forces could be developed based on kinematics and dynamics. Thirdly, the dynamic cutting force model and the chatter stability of the machining system could be investigated for further improvement of surface quality. Since the cutting forces are directly loaded on the machined surface, the frequency and amplitude of vibrations will influence the micro texture such as the waviness and roughness of the machined surface.

Acknowledgement

This work is supported by the National Natural Science Foundation of China (Grant No.51535007 and 51775343). The authors are grateful to Shanghai Automotive Industry Corporation General Motors Wuling Company in Liuzhou, China, for providing the B12 engine blocks for experiments.

Appendix A

Derivation of Eq. (43):

Substituting Eq. (40) into Eq. (38), yields

$$\epsilon_r = -\frac{2P \cos \theta}{\pi Er} \tag{A.1}$$

$$\epsilon_\theta = \frac{2\nu P \cos \theta}{\pi Er} \tag{A.2}$$

$$\gamma_{r\theta} = 0 \tag{A.3}$$

Substituting the above equations into Eq. (37), yields

$$\frac{\partial u}{\partial r} = -\frac{2P \cos \theta}{\pi Er} \tag{A.4}$$

$$\frac{\partial v}{r \partial \theta} + \frac{u}{r} = \frac{2\nu P \cos \theta}{\pi Er} \tag{A.5}$$

$$\frac{\partial v}{\partial r} + \frac{\partial u}{r \partial \theta} - \frac{v}{r} = 0 \tag{A.6}$$

Equation Eq. (A.4) can be rewritten as

$$u = \int \varepsilon_r dr = -\frac{2P}{\pi E} \ln r \cos \theta + g(\theta) \quad (\text{A.7})$$

where $g(\theta)$ is a function of variable θ .

Substituting Eq. (A.7) into Eq. (A.5), yields

$$v = \int (r\varepsilon_\theta - u)d\theta = \frac{2\nu P}{\pi E} \sin \theta + \frac{2P}{\pi E} \sin \theta \ln r - G(\theta) + f(r) \quad (\text{A.8})$$

where $G(\theta)$ is the primitive of $g(\theta)$, while $f(r)$ is a function of variable r .

Substituting Eq. (A.7) and Eq. (A.8) into Eq. (A.6), it can be further derived that

$$\frac{2(1-\nu)P}{\pi E} \sin \theta + g'(\theta) + G(\theta) = f(r) - rf'(r) \quad (\text{A.9})$$

To keep Eq. (A.9) always valid, both side of this equation shall be 0.

By solving two ordinary differential equations, the general solutions to $f(r)$ and $g(\theta)$ are obtained respectively:

$$f(r) = C_1 r \quad (\text{A.10})$$

$$g(\theta) = -\frac{(1-\nu)P}{\pi E} \sin \theta + C_2 \sin \theta + C_3 \cos \theta \quad (\text{A.11})$$

where C_1 , C_2 and C_3 are undetermined constant coefficients.

Therefore, the displacement field can be represented as

$$u = -\frac{2P}{\pi E} \ln r \cos \theta - \frac{(1-\nu)P}{\pi E} \sin \theta + C_2 \sin \theta + C_3 \cos \theta \quad (\text{A.12})$$

$$v = \frac{2P}{\pi E} (\ln r + \nu) \sin \theta + \frac{(1-\nu)P}{\pi E} (\sin \theta - \theta \cos \theta) + C_2 \cos \theta - C_3 \sin \theta + C_1 r \quad (\text{A.13})$$

To calculate above three constant coefficients, considering the boundary conditions shown in Fig. 13, the horizontal displacement remains 0 for all mass points on the X-axis.

$$v|_{\theta=0} = C_2 + C_1 r = 0 \quad (\text{A.14})$$

Thus $C_1 = C_2 = 0$.

The vertical displacement of the mass points on the X-axis can be expressed as

$$u|_{\theta=0} = -\frac{2P}{\pi E} \ln r + C_3 \quad (\text{A.15})$$

For an elastic sheet loaded by a vertical concentrated force on its straight boundary, if the vertical extent is sufficiently long, the influence range of the load will be limited. Since d_B denotes the minimum distance between the local coordinate origin and the point on X-axis whose vertical displacement is 0, it can be derived that

$$u|_{\theta=0, r=d_B} = -\frac{2P}{\pi E} \ln d_B + C_3 = 0 \quad (\text{A.16})$$

Thus $C_3 = \frac{2P}{\pi E} \ln d_B$.

References

- [1] Du SC, Liu T, Huang DL. A fast and adaptive Bi-dimensional empirical mode decomposition approach for filtering of workpiece surfaces using high definition metrology. *J Manuf Syst* 2018;46:247–63.
- [2] Zeng SS, Wan XJ, Li WL, Yin ZP, Xiong YL. A novel approach to fixture design on suppressing machining vibration of flexible workpiece. *Int J Mach Tool Manufact* 2012;58:29–43.
- [3] Wan XJ, Zhang Y, Huang XD. Investigation of influence of fixture layout on dynamic response of thin-wall multi-framed work-piece in machining. *Int J Mach Tool Manufact* 2013;75:87–99.
- [4] Hashemi H, Shaharoun AM, Sudin I. A case-based reasoning approach for design of machining fixture. *Int J Adv Manuf Technol* 2014;74:113–24.
- [5] Meshreki M, Kóvecses J, Attia H. Dynamics modeling and analysis of thin-walled aerospace structures for fixture design in multi-axis milling. *J Manuf Sci Eng* 2008;130. 031011-1-12.
- [6] Tonietti G, Schiavi R, Bichi A. “Design and control of a variable stiffness actuator for safe and fast physical human/robot interaction. International conference on robotics and automation, proceedings of the 2005 IEEE. 2005. p. 526–31.
- [7] Alblalaid K, Lawes S, Kinnell P. Variable stiffness probing systems for micro-coordinate measuring machines. *Precis Eng* 2016;43:262–9.
- [8] Varadarajan N, Nagarajaiah S. Wind response control of building with variable stiffness tuned mass damper using empirical mode decomposition/hilbert transform. *J Eng Mech* 2004;130(4):451–8.
- [9] Du SC, Fei L. Co-kriging method for form error estimation incorporating condition variable measurements. *J Manuf Sci Eng* 2016;138. 041003-1-16.
- [10] Wang M, Xi LF, Du SC. 3D surface form error evaluation using high definition metrology. *Precis Eng* 2014;38(1):230–6.
- [11] Du SC, Liu CP, Huang DL. A shearlet-based separation method of 3D engineering surface using high definition metrology. *Precis Eng* 2015;40:55–73.
- [12] Vasundara M, Padmanaban KP. Recent developments on machining fixture layout design, analysis, and optimization using finite element method and evolutionary techniques. *Int J Adv Manuf Technol* 2014;70:79–96.
- [13] Yi SN, Xu L, Cheng GD. FEM formulation of homogenization method for effective properties of periodic heterogeneous beam and size effect of basic cell in thickness direction. *Comput Struct* 2015;156:1–11.
- [14] Huang DL, Du SC, Li GL. A systematic approach for on-line minimizing volume difference of multiple chambers in machining processes based on high definition metrology. *J Manuf Sci Eng* 2017;139(8). 081003-1-17.
- [15] Yi SN, Cheng GD, Xu L. Stiffness design of heterogeneous periodic beam by topology optimization with integration of commercial software. *Comput Struct* 2016;172:71–80.
- [16] Cai W, Hu SJ. Deformable sheet metal fixturing: principles, algorithms, and simulations. *J Manuf Sci Eng* 1996;118:318–24.
- [17] Liu SG, Zheng L, Zhang ZH. Optimal fixture design in peripheral milling of thin-walled workpiece. *Int J Adv Manuf Technol* 2006;28:653–8.
- [18] Chen WF, Ni LJ, Xue JB. Deformation control through fixture layout design. *Int J Adv Manuf Technol* 2008;38:860–7.
- [19] Rai JK, Xirouchakis P. Finite element method based machining simulation environment for analyzing Part Errors induced during milling of thin-walled components. *Int J Mach Tool Manufact* 2008;48:629–43.
- [20] Bellifa H, Benrahou KH, Hadji L. Bending and free vibration analysis of functionally graded plates using a simple shear deformation theory and the concept the neutral surface position. *J Braz Soc Mech Sci Eng* 2016;38:265–75.
- [21] Ebrahimi F, Barati MR. A nonlocal higher-order shear deformation beam theory for vibration analysis of size-dependent functionally graded nanobeams. *Arabian J Sci Eng* 2016;41:1679–90.

- [22] Shan C, Lv X, Duan W. Effect of tool inclination angle on the elastic deformation of thin-walled parts in multi-axis ball-end milling. *Procedia CIRP* 2016;56:311–5.
- [23] Kaya N, Ozturk F. The application of chip removal and frictional contact analysis for workpiece-fixture layout verification. *Int J Adv Manuf Technol* 2003;21(6):411–9.
- [24] Carlson JS. Quadratic sensitivity analysis of fixtures and locating schemes for rigid parts. *J Manuf Sci Eng* 2001;123:462–72.
- [25] Sadd MH. Some simple cartesian solutions to plane non-homogeneous elasticity problems. *Mech Res Commun* 2010;37:22–7.
- [26] Pimenov DY, Guzeev VI, Krolczyk G, Mia M, Wojciechowski S. Modeling flatness deviation in face milling considering angular movement of the machine tool system components and tool flank wear. *Precis Eng* 2018;54:327–37.
- [27] Wojciechowski S. Machined surface roughness including cutter displacements in milling of hardened teal. *Metrol Meas Syst* 2011;18(3):429–40.
- [28] Kang Y, Rong Y, Yang JA. Geometric and kinetic model based computer-aided fixture design verification. *J Comput Inf Sci Eng* 2003;3:187–99.
- [29] Kang Y, Rong Y, Yang JC. Computer-aided fixture design verification. Part 1. The framework and modelling. *Int J Adv Manuf Technol* 2003;21:827–35.
- [30] Liao YG, Hu SJ. Flexible multibody dynamics based fixture-workpiece analysis model for fixturing stability. *International Journal of Machine Tools & Manufacturing* 2000;40:343–62.
- [31] Liao YG, Hu SJ. “An integrated model of a fixture–workpiece system for surface quality prediction. *Int J Adv Manuf Technol* 2001;17:810–8.
- [32] Gong X, Lu Q, Wang Y, Song Y. Mechanical design and finite element analyses of surface bending mechanism for X-ray optics. *Precis Eng* 2018;53:107–19.
- [33] Doostie S, Hoshiar AK, Nazarahari M, Lee S, Choi H. Optimal path planning of multiple nanoparticles in continuous environment using a novel adaptive genetic algorithm. *Precis Eng* 2018;53:65–78.
- [34] Lai HY, Jywe WY, Chen CK, Liu CH. Precision modeling of form errors for cylindricity evaluation using genetic algorithms. *Precis Eng* 2000;24:310–9.
- [35] Qiu MK, Ming Z, Li JY, Gai KK, Zong ZL. Phase-change memory optimization for green cloud with genetic algorithm. *IEEE Trans Comput* 2015;64(12):3528–40.
- [36] Krishnakumar K, Melkote SN. Machining fixture layout optimization using the genetic algorithm. *Int J Mach Tool Manufact* 2000;40:579–98.
- [37] Timoshenko SP, Goodier JN. *Theory of elasticity*. New York: McGraw-Hill Book Co.; 1934.
- [38] Du SC, Liu T, Huang DL. An optimal ensemble empirical mode decomposition method for vibration signal decomposition. *J Vib Acoust* 2017;139. 031003-1-18.
- [39] Suriano S, Wang H, Shao CH, Hu SJ, Sekhar P. Progressive measurement and monitoring for multi-resolution data in surface manufacturing considering spatial and cross correlations. *IIE Trans* 2015;47:1033–52.
- [40] Du SC, Liu CP, Xi LF. A selective multiclass support vector machine ensemble classifier for engineering surface classification using high definition metrology. *J Manuf Sci Eng* 2015;137(1):011003.
- [41] Du SC, Huang DL, Wang H. “An adaptive support vector machine-based workpiece surface classification system using high-definition metrology,” instrumentation and measurement. *IEEE Transactions on* 2015;64(10):2590–604.
- [42] Shirase K, Altintas Y. Cutting force and dimensional surface error generation in peripheral milling with variable pitch helical end mills. *Int J Mach Tool Manufact* 1996;36(5):567–84.
- [43] Ko JH, Cho DW. 3D ball-end milling force model using instantaneous cutting force coefficients. *J Manuf Sci Eng* 2005;127:1–12.
- [44] Wan M, Zhang WH, Dang JW, Yang Y. New procedures for calibration of instantaneous cutting force coefficients and cutter runout parameters in peripheral milling. *Int J Mach Tool Manufact* 2009;49:1144–51.
- [45] Wan M, Pan WJ, Zhang WH, Ma YC, Yang Y. A unified instantaneous cutting force model for flat end mills with variable geometries. *J Mater Process Technol* 2014;214:641–50.
- [46] Li B, Melkote SN. Fixture clamping force optimization and its impact on workpiece location accuracy. *Int J Adv Manuf Technol* 2001;17:104–13.
- [47] Roy U, Liao J. Fixturing analysis for stability consideration in an automated fixture design system. *J Manuf Sci Eng* 2002;124:98–104.
- [48] Varadarajan KM, Culpepper ML. A dual-purpose positioner-fixture for precision six-axis positioning and precision fixturing Part II. Characterization and calibration. *Precis Eng* 2007;31:287–92.
- [49] Wang M, Shao YP, Du SC, Xi LF. A diffusion filter for discontinuous surface measured by high definition metrology. *Int J Precis Eng Manuf* 2015;16(10):2057–62.
- [50] Wang J, Yu T, Ding W, Fu Y, Bastawros AF. Wear evolution and stress distribution of single CBN superabrasive grain in high-speed grinding. *Precis Eng* 2018;54:70–80.
- [51] Arola D, Williams CL. Estimating the fatigue stress concentration factor of machined surfaces. *Int J Fatig* 2002;24:923–30.
- [52] Sbularti R. Stress concentration factor due to a functionally graded ring around a hole in an isotropic plate. *Int J Solid Struct* 2013;50:3649–58.
- [53] Tang AJ, Liu ZQ. Deformations of thin-walled plate due to static end milling force. *J Mater Process Technol* 2008;206:345–51.
- [54] Zhang HY, Wang MY, Li J, Zhu J. A soft compressive sensor using dielectric elastomers. *Smart Mater Struct* 2016;25(3). 035045-1-7.
- [55] Field FA. A comment on the uniqueness of the solution to boussinesq's problem. *J Appl Mech* 1964;31(3):547.
- [56] Gao X, Hao F, Fang DN, Huang ZP. Boussinesq problem with the surface effect and its application to contact mechanics at the nanoscale. *Int J Solid Struct* 2013;50:2620–30.
- [57] Kaya N. Machining fixture locating and clamping position optimization using genetic algorithms. *Comput Ind* 2006;57:112–20.
- [58] Wang S, Rong W, Wang L, Pei Z, Sun L. A novel inchworm type piezoelectric rotary actuator with large output torque: design, analysis and experimental performance. *Precis Eng* 2018;51:545–51.
- [59] Hughes TJR. *The finite element method: linear static and dynamic finite element analysis*. New Jersey: Prentice-Hall, Inc.; 1987.